JACS
JOURNAL OF THE AMERICAN CHEMICAL SOCIETY
Article
pubs.acs.org/JACS

# Electronic Structure of an [FeFe] Hydrogenase Model Complex in Solution Revealed by X-ray Absorption Spectroscopy Using Narrow-Band Emission Detection

Nils Leidel,[†] Petko Chernev,[†] Kajsa G. V. Havelius,[†] Lennart Schwartz,[‡] Sascha Ott,[‡] and Michael Haumann*[,†]

[†]Institut für Experimentalphysik, Freie Universität Berlin, 14195 Berlin, Germany

[‡]Department of Chemistry, Uppsala University, Ångström Laboratories, 75120 Uppsala, Sweden

Supporting Information

**ABSTRACT:** High-resolution X-ray absorption spectroscopy with narrow-band X-ray emission detection, supported by density functional theory calculations (XAES-DFT), was used to study a model complex, ($[Fe_2(\mu\text{-adt})(CO)_4(PMe_3)_2]$ (**1**, adt = S−$CH_2$−$(NCH_2Ph)$−$CH_2$−S), of the [FeFe] hydrogenase active site. For **1** in powder material ($\mathbf{1}_{powder}$), in MeCN solution (**1′**), and in its three protonated states (**1H**, **1Hy**, **1HHy**; **H** denotes protonation at the adt−N and **Hy** protonation of the Fe−Fe bond to form a bridging metal hydride), relations between the molecular structures and the electronic configurations were determined. EXAFS analysis and DFT geometry optimization suggested prevailing rotational isomers in MeCN, which were similar to the crystal structure or exhibited rotation of the (CO) ligands at Fe1 ($\mathbf{1}_{CO}$, $\mathbf{1Hy}_{CO}$) and in addition of the phenyl ring ($\mathbf{1H}_{CO,Ph}$, $\mathbf{1HHy}_{CO,Ph}$), leading to an elongated solvent-exposed Fe−Fe bond. Isomer formation, adt−N protonation, and hydride binding caused spectral changes of core-to-valence (pre-edge of the Fe K-shell absorption) and of valence-to-core (Kß$^{2,5}$ emission) electronic transitions, and of K$\alpha$ RIXS data, which were quantitatively reproduced by DFT. The study reveals (1) the composition of molecular orbitals, for example, with dominant Fe-d character, showing variations in symmetry and apparent oxidation state at the two Fe ions and a drop in MO energies by ∼1 eV upon each protonation step, (2) the HOMO−LUMO energy gaps, of ∼2.3 eV for $\mathbf{1}_{powder}$ and ∼2.0 eV for **1′**, and (3) the splitting between iron d($z^2$) and d($x^2-y^2$) levels of ∼0.5 eV for the nonhydride and ∼0.9 eV for the hydride states. Good correlations of reduction potentials to LUMO energies and oxidation potentials to HOMO energies were obtained. Two routes of facilitated bridging hydride binding thereby are suggested, involving ligand rotation at Fe1 for $\mathbf{1Hy}_{CO}$ or adt−N protonation for $\mathbf{1HHy}_{CO,Ph}$. XAES-DFT thus enables verification of the effects of ligand substitutions in solution for guided improvement of [FeFe] catalysts.

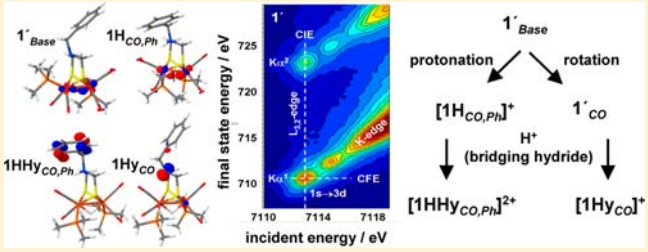


## INTRODUCTION

Hydrogen ($H_2$) is expected to play an important role in the energy economy of the future as a renewable fuel derived in solar-powered facilities.[1−5] The development of effective and long-lived catalysts for $H_2$ generation thus is a key in the transition to a hydrogen economy, but represents a significant scientific challenge.[6−8] In nature, efficient $H_2$ catalysts are found in the form of hydrogenase enzymes, which contain transition metal ions, that is iron and nickel, as essential ingredients of their active sites.[9−11] The paramount $H_2$ producing enzymes with reported turnover rates of up to $10^4$ $s^{-1}$ are the [FeFe] hydrogenases,[12] which are found in bacteria and green algae.[13,14] Their active site is an unusual six-iron complex denoted as H-cluster (Figure 1). It comprises a catalytically active binuclear site ($2Fe_H$), which is linked to a [4Fe4S] cluster that is part of the electron transfer chain to the active site.[15,16] The binuclear [FeFe] unit carries unusual carbon monoxide (CO) and cyanide ($CN^-$) ligands[17,18] and a bridging dithiolate species, which presumably is an azadithiolate (adt) group.[19,20] A major obstacle for the use of [FeFe] hydrogenases in biotechnological $H_2$ production, however, is the high sensitivity of the enzymes toward irreversible inhibition by $O_2$.[21−23] Improvement of the enzymes by, for example, protein engineering,[24,25] may be expected to result from the combination of insights into the natural system and synthetic models of the active site.

In past decades, synthetic chemistry has been extraordinarily successful in the preparation of a variety of [FeFe] model complexes, which mimic important features of the $2Fe_H$ site in the enzymes.[20,26−38] These diiron compounds were designed to explore features of the metal sites, which are believed to be crucial for the $H_2$ reactivity also in the enzymes, such as variations of the iron ligands and coordination geometry, of protonation changes at, for example, the bridging dithiolate group, and in particular, of the formation of metal-bound

**Received:** May 22, 2012
**Published:** August 3, 2012

   dx.doi.org/10.1021/ja304970p | J. Am. Chem. Soc. 2012, 134, 14142−14157

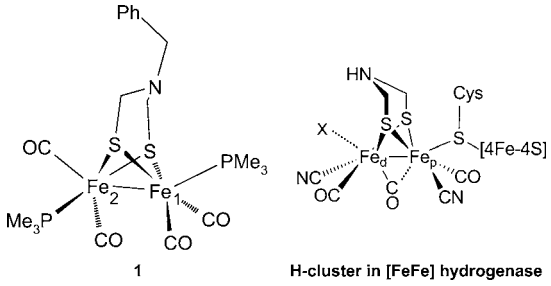


**Figure 1.** Schematic drawing of the structure of complex **1**[82] ([$Fe_2$($\mu$-adt)$(CO)_4(PMe_3)_2$], adt = S−$CH_2$−($NCH_2$Ph)−$CH_2$−S) and of the active-site H-cluster of [FeFe] hydrogenase. The H-cluster comprises a binuclear unit ($2Fe_H$) and an iron−sulfur cluster ([4Fe4S]).[15,18,21,102,114,115] It may contain a bridging carbonyl connecting the proximal (p) and distal (d) iron atoms, a yet unidentified ligand (X) at $Fe_p$ in the oxidized state, and a nitrogen atom in an azadithiolate bridge;[19] Cys denotes a cysteine side chain from the protein. Protons were omitted except for the adt−NH for clarity. For **1**, Fe1 denotes the iron atom closest to the nitrogen atom of the adt.

hydride species.[39−46] Unfortunately, so far the turnover rates and numbers of synthetic [FeFe] catalysts as well as their stability mostly are too low for technical applications.[47] These shortcomings may be overcome by improving the characterization of molecular and electronic structures of intermediates, which are formed under reaction conditions, that is, in solution. Another point is that built-in chemical changes may not lead to the desired properties under solution conditions, due to, for example, formation of rotational isomers. In addition, the properties of hydride binding intermediates are at the center of interest, but difficult to study by spectroscopic methods.[48−52] Therefore, novel experimental techniques are required, by which structural and electronic information on [FeFe] compounds in all states in solution can be determined.

Synchrotron-based X-ray spectroscopy methods such as X-ray absorption and emission spectroscopy, XAS and XES, and resonant inelastic X-ray scattering, RIXS, in principle allow one to study all states of [FeFe] compounds, that is, not restricted to certain spin or oxidation states, in solid material as well as under solution conditions.[53−57] Most informative is the combination of high-resolution XAS and narrow-band detection XES in a single experiment (XAES).[53,54,58−64] This approach specifically deduces structural features such as interatomic distances, site geometry, and ligation patterns, and the electronic configuration, for example, metal oxidation state and orbital energies, occupancies, and interactions, in an eventually even spin- and site-selective fashion.[53,58,65−71] Recently, several authors, including our group, have focused on the employment of XAES to characterize a considerable variety of iron compounds.[58,65,72−79] The calculation of XAES spectra by density functional theory (DFT) methods has been established, in particular for emission features due to valence-to-core transitions (e.g., Kß$^{2,5}$ emission) and for absorption features due to core-to-valence transitions (e.g., pre-edge peaks of the metal K-edge).[58,72,74] The XAES-DFT approach has facilitated site-selective determination of parameters of the individual Fe ions in an asymmetric [FeFe] hydrogenase model[58] and allowed for the assignment as a carbon of the central atom in the iron−molybdenum cofactor of nitrogenase protein.[80,81]

In the present XAES-DFT investigation, we studied an [FeFe] hydrogenase active site model complex (**1**; [$Fe_2$($\mu$-adt)$(CO)_4(PMe_3)_2$], adt = S−$CH_2$−($NCH_2$Ph)−$CH_2$−S)[82] (Figure 1) in four distinct states in acetonitrile (MeCN) solution, that is, unprotonated (**1′**), protonated at either the adt−N (**1H**) or the Fe−Fe bond (**1Hy**), or at both positions (**1HHy**) (Figure 2),[49,52,82] and compared the obtained results

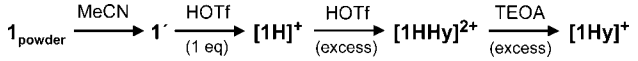


**Figure 2.** Formation of three protonation states of complex **1** in MeCN solution in response to the addition of acids (HOTf, triflic acid; TEOA, triethanolamine), as established previously.[52,82] The first step denotes the dissolution of powder material ($\mathbf{1}_{powder}$) in MeCN (acetonitrile) to yield the unprotonated **1′**; [**1H**]$^+$ is protonated at the adt−N, [**1Hy**]$^+$ holds an Fe−Fe bridging formal hydride ($H^-$), and [**1HHy**]$^{2+}$ is protonated at both sites.

to those from the unprotonated complex in powder material ($\mathbf{1}_{powder}$) and in the crystal structure ($\mathbf{1}_{crystal}$).[82] Complex **1** comprises several features that are believed to be essential for the function in [FeFe] hydrogenase active sites, a pendant nitrogen base at the azadithiolate ligand, iron coordination by electron-rich CO and $PMe_3$ groups (the latter replacing the $CN^-$ ligands in the H-cluster), and the ability to form an iron-hydride (Fe−$H^-$) bond and to liberate $H_2$ in electrochemical experiments.[52]

For **1**, sets of iron X-ray emission line spectra were recorded, which reflect the various radiative electronic decay processes (K$\alpha^{1(2)}$, $2p_{3/2(1/2)}$→1s; Kß$^{1,3}$(Kß′), 3p→1s; Kß$^{2,5}$, valence-to-core transitions, for example, 3d→1s), refilling the core hole created upon the previous X-ray excitation. The latter process was followed by collecting X-ray absorption spectra due to promotion of a 1s electron resonantly into bound levels (core-to-valence transitions, e.g., 1s→3d; resonant inelastic X-ray scattering, RIXS, allowing for measuring of L-edge type spectra using hard X-ray excitation) or nonresonantly into the continuum (EXAFS). Our XAES-DFT results facilitate discrimination of main rotational isomer species in solution, reveal the effects of dithiolate ligand protonation, and specifically probe the hydride binding. This has led to an improved understanding of the relations between the molecular and electronic structures of complex **1**, in particular with respect to inherent asymmetry at its two iron sites.

## MATERIALS AND METHODS

**Synthesis and Sample Preparation Procedures.** Complex **1** was synthesized and prepared in its unprotonated form and its three protonation states (>95%) in MeCN solution (5 mM of complex **1**) as previously described (Figure 2).[49,52,82] The crystal structure of compound **1** has been reported elsewhere.[82] Powder material of **1** was homogeneously diluted with solid boron nitride. Powder and solution samples were filled into Kapton-covered Delrin sample holders for XAES and immediately frozen in liquid nitrogen.[49]

**X-ray Experiments.** X-ray spectroscopy was carried out at the undulator beamline ID26 of the European Synchrotron Radiation Facility (ESRF) at Grenoble (France) as previously.[58,76] Samples were held in a laboratory-built liquid-He cryostat at 20 K. The incident energy was set by an Si[311] double-crystal monochromator (energy bandwidth ~0.2 eV at the Fe K-edge). Conventional EXAFS spectra were collected by monitoring the K$\alpha$ fluorescence using a scintillation detector (~20 $cm^2$ area, placed at 90° to the incident X-ray beam and at ~1 m to the sample), which was shielded by 10 $\mu$m Mn foil against scattered incident X-rays. EXAFS oscillations were extracted as described[83] ($E_0$ of 7112 eV). Unfiltered $k^3$-weighted spectra were used for least-squares multiple-scattering curve-fitting and Fourier-transform (FT) calculation with the program SimX.[83] EXAFS phase-


dx.doi.org/10.1021/ja304970p | J. Am. Chem. Soc. 2012, 134, 14142−14157

functions were calculated with FEFF8 (group of J. J. Rehr, University of Washington[83]). $E_0$ was refined to ~7120 eV in the EXAFS fits (amplitude reduction factor, $S_0^2$, of 0.85). High energy-resolution emission detection was achieved by using a vertical-plane Rowland-circle spectrometer and a silicon-drift detector for monitoring of the X-ray fluorescence. Total energy bandwidths of ~1.3 or ~1.0 eV at the Fe Kα or Kß fluorescence lines were achieved using the [440] (Kα) or [620] (Kß) Bragg reflections of five spherically bent Ge wafers ($R$ = 1000 mm). The energy axes of the monochromator and emission spectrometer were calibrated (accuracy ±0.1 eV) as outlined elsewhere.[58] Kα and Kß emission line spectra were collected for off-resonance excitation at 7700 eV. XANES spectra at the Fe K-edge were measured using the rapid-scan mode of ID26 and, in parallel, narrow-band Kα emission detection and total-fluorescence detection with a large-area scintillation detector. For collection of RIXS plane data, the emission detection energy for XANES measurements was varied over the Kα spectral region in 0.3 eV steps; RIXS data were averaged and evaluated using in-house Matlab (Mathsoft) tools. After signal averaging, XANES spectra were normalized to an edge jump of unity, and the pre-edge region was isolated using the subtraction of a polynomial spline through the main edge rise.[83] For a schematic depiction of the setup and further technical details of the X-ray experiments, see ref 58.

**Density Functional Theory Calculations.** Geometry optimization of [FeFe] model structures and spin-unrestricted single-point calculations were performed with the DFT program package ORCA.[84] The BP86 exchange correlation functional[85−87] and a triple-ζ valence plus polarization (TZVP) basis set[88] were used. For the solution structures, which were derived after appropriate modification of the crystal structure of the unprotonated complex,[82] a COSMO solvation model[89] with a dielectric constant of $\varepsilon$ = 46 for acetonitrile[89] was used in the geometry optimizations. Structures of **1** were used with a singlet ground state and appropriate total charge of 0 (unprotonated), 1+ (protonated at either the adt−N or the Fe−Fe bond) or 2+ (protonated at the adt−N and the Fe−Fe bond). The resulting MOs were visualized as isosurfaces with the programs Jmol or UCSF Chimera. The contributions of individual Fe-d atomic orbitals to the MOs were determined from calculations on appropriately oriented model structures (see below), using Mulliken population analysis.[90] For each Fe atom, the coordinate system was oriented in a way that the $x$- and $y$-axes pointed roughly from the Fe atom to the two S atoms; the $z$-axis accordingly points in the direction of the Fe−H bond (i.e., for the hydride states). X-ray absorption K-edge intensities in the pre-edge region (core-to-valence transitions) were calculated using a time-dependent DFT (TD-DFT) formalism,[73,91] and Kß valence-to-core transitions (Kß$^{2,5}$ emission) were calculated using the DFT approach described in refs 72,78 (see also ref 58). A spin multiplicity of $M$ = 1 was employed in both calculation procedures. A shift to higher energies by 181.35 eV and, if not otherwise stated, a 1.0 eV Gaussian broadening of stick spectra were applied to calculated Kß emission lines and pre-edge absorption spectra for comparison with the experimental data. For further computational details, see ref 58.

## RESULTS

**The Unprotonated Complex 1 and Its Three Protonated States in MeCN Solution.** Complex **1** (Figure 1) was prepared in its four states by dissolution of powder material ($\mathbf{1}_{powder}$) in acetonitrile (MeCN) and the addition of acids according to established procedures[49,52,82] (Figure 2). The solution samples are denoted **1′**, unprotonated state of **1**; $[\mathbf{1H}]^+$, protonated at the adt−N; $[\mathbf{1Hy}]^+$, containing a bridging hydride; and $[\mathbf{1HHy}]^{2+}$ with a protonated adt−N and a bridging hydride. The complex charges are hereafter neglected for simplicity. Quantitative formation (>95%) of the different protonation states was verified by infrared spectroscopy (not shown, see refs 49,82). In cases where the adt−N is protonated (as in **1H** and **1HHy**), inversion of the six-membered $FeS_2C_2N$ metalloazaheterocycles is restricted on the NMR time scale at room temperature, as evident for example by the emergence of two $^{31}$P NMR signals for the $PMe_3$ ligands.[82] This restricted rotation renders the two Fe centers in **1H** and **1HHy** nonequivalent. For **1** and **1Hy**, the respective $FeS_2C_2N$ metalloazaheterocycle inversion is restricted due to the low temperatures that were used for this study. Thus, a differentiation between the two Fe centers is possible in all protonation states described herein. The iron atom that resides under the adt nitrogen is denoted Fe1, and the other more exposed iron is referred to as Fe2 (Figure 1).

**Rotational Isomers in Solution Suggested by EXAFS and DFT.** EXAFS was employed to determine the basic structural parameters of the [FeFe] complex in powder material ($\mathbf{1}_{powder}$) and MeCN solution (**1′**) in comparison to the crystal structure ($\mathbf{1}_{crystal}$). The resulting EXAFS spectra (Figure S1) were simulated using a multiple-scattering (ms) approach,[22,49] which involved Fe−C(=O), Fe−S/P, Fe−Fe, and Fe(−C)=O$_{ms}$ interactions (Table S1). The determined Fe−Fe distances and mean Fe−ligand bond lengths are summarized in Figure 3.

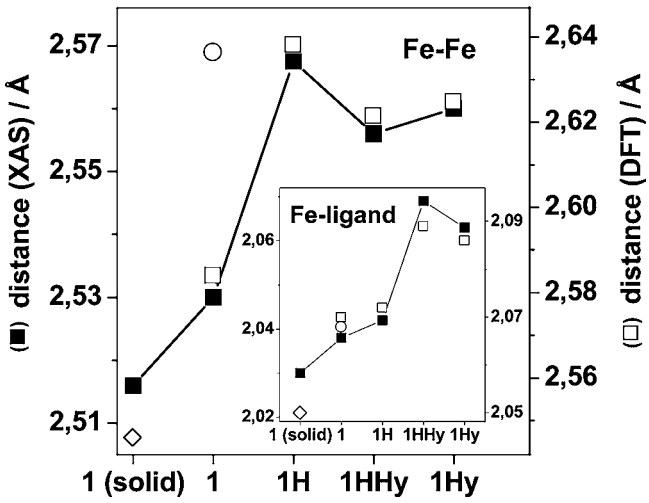


**Figure 3.** Structural parameters from EXAFS. Fe−Fe distances and mean Fe−ligand bond lengths in the inset (■) as determined from EXAFS analysis (left $y$-axis, see Figure S1 and Table S1) are compared to respective values from DFT-calculated structures (right $y$-axis). Values from DFT correspond to structures $\mathbf{1}_{Base}$, $\mathbf{1H}_{CO,Ph}$, $\mathbf{1HHy}_{CO,Ph}$, and $\mathbf{1Hy}_{CO}$ (□) and $\mathbf{1}_{CO}$ (○); values for $\mathbf{1}_{crystal}$[82] are shown as "◇".

The EXAFS analysis reveals structural changes of complex **1** due to adt−N protonation and hydride binding in MeCN, confirming previous results[49] (Figure 3). Minor distance differences are due to the shorter $k$-range of EXAFS data in the present study. In particular, a pronounced increase by ~0.05 Å of the Fe−Fe distance in **1H**, **1HHy**, and **1Hy**, and an increase by ~0.03 Å of the mean Fe−ligand distance only in **1HHy** and **1Hy** are observed. A slight increase of the interatomic distances in MeCN was found for **1′** as compared to $\mathbf{1}_{powder}$. These changes are remarkably well reproduced by the respective model structures from DFT calculations (Figure 3).

According to the crystal structure of complex **1**[82] (Figure 1) and previous $^1$H and $^{31}$P NMR results,[52,82] several isomers of the crystallographic configuration may be formed in solution (Supporting Information, Figure S2). An overall orientation of the phenyl ring and of the ligands at Fe1 similar to the one in the crystal structure (Figure 1) further on is denoted "Base",

that is, $\mathbf{1}_{Base}$. Rotation of the phenyl ring is denoted "Ph", that is, $\mathbf{1}_{Ph}$. Rotation of the $(CO)_2(PMe_3)$ ligands at Fe1 is denoted "CO", that is, $\mathbf{1}_{CO}$, and brings the $PMe_3$ ligand in a basal and a CO in an apical position, in contrast to the situation at Fe1 in the crystal structure. A combination of both rotations is denoted "CO,Ph", that is, $\mathbf{1}_{CO,Ph}$. Rotations at Fe2 were not considered because they were too high in energy to be formed in relevant quantities according to the DFT results. Sixteen geometry-optimized structures with different rotational conformations of particular functional groups (four isomers of four protonation states) were calculated by DFT. Significant changes of their total energy ($\Delta E_{tot}$) ranging between about +70 and −300 meV were observed for the different configurations (Table 1).

**Table 1. Energies of Rotational Isomers of Complex 1 in MeCN Solution**[a]

| | $\Delta E_{tot}$ [eV] | | | |
|---|---|---|---|---|
| | **1** | **1H** | **1HHy** | **1Hy** |
| Base | 0 | 0 | 0 | 0 |
| Ph | 0.039 | −0.041 | −0.007 | 0.066 |
| CO | **0.014** | −0.185 | −0.213 | **−0.111** |
| CO,Ph | 0.031 | **−0.231** | **−0.301** | −0.057 |

[a]Energy differences ($\Delta E_{tot}$) between structures for the crystal configuration (Base) and three isomers (Figure 4) for the unprotonated and protonated states of complex **1** were derived from DFT. The energy of $\mathbf{1}_{Base}$ was set to zero. Bold numbers mark the apparently most abundant species in MeCN solution.

The isomers with lowest energies in Table 1 are consistent with the favored isomers found in previous NMR, XAS, and DFT studies.[49,52,82] Accordingly, $\mathbf{1}_{Base}$, $\mathbf{1}_{CO}$, $\mathbf{1H}_{CO,Ph}$, $\mathbf{1HHy}_{CO,Ph}$, and $\mathbf{1Hy}_{CO}$ were expected to be the most abundant species in MeCN. When taking the $\Delta E$ values in Table 1 simply as the free energy differences of the rotations, this suggested relative concentrations of the main species of up to about 50%. However, at least for the protonated states, the experimental data are compatible with close to 100% populations of the main species, likely due to additional energetic barriers in the rotation paths. The corresponding DFT-optimized structures of the main solution species are compared to the crystal structure in Figure 4. Protonation at the adt−N, irrespective of the presence or absence of the bridging hydride, locks the structure in a configuration with CO rotation at Fe1, due to the formation of a hydrogen bond between the apical CO group at Fe1 and the adt−NH.[49,52,82] For the unprotonated adt−N, the Base (for **1′**) or CO (for **1Hy**) configurations are preferred. Phenyl-rotation (Ph) affects the energies only slightly. In the following, we will restrict the XAES-DFT analysis to the apparently most abundant solution structures in comparison to the structures of **1** in powder and crystalline material.

### X-ray Fluorescence Emission Line (XES) Spectra of 1.

XES spectra in three different regions due to nonresonant excitation of the solution and powder samples of complex **1** are shown in Figure 5, together with the underlying electronic decay processes. Relatively small but reproducible changes of the emission line energies and shapes were observed (Figure 5, insets).

The K$\alpha^1$ line (Figure 5A) of **1′** was at slightly lower energies as compared to $\mathbf{1}_{powder}$; adt−N protonation caused negligible line shifts, but the line was up-shifted by ∼0.1 eV for **1HHy** and **1Hy**. For the Kß spectra, the absence of an emission peak in the Kß′ region (Figure 5B) revealed the absence of unpaired spins and the low-spin character of both iron atoms in all states of **1**.[58] The Kß$^{1,3}$ line was at lower energies for **1′** as compared to $\mathbf{1}_{powder}$; adt−N protonation again caused small line shifts, but hydride binding in **1HHy** and **1Hy** resulted in a sizable upshift

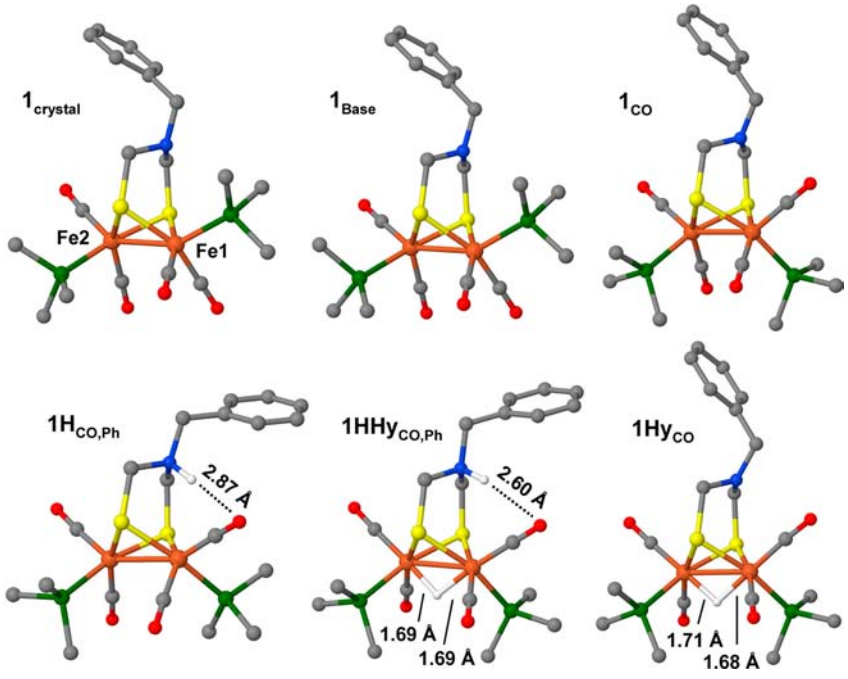


**Figure 4.** Geometry-optimized solution structures of complex **1** from DFT calculations as compared to the crystal structure ($\mathbf{1}_{crystal}$). The lengths of the hydrogen bond between the rotated apical CO group at Fe1 and the adt−N and the distances of the bridging hydride to the Fe ions are indicated. Color code: orange, Fe; red, O; blue, N; yellow, S; green, P; gray, C; protons except for the Fe−H−Fe and adt−NH motifs were omitted in the drawings for clarity.


dx.doi.org/10.1021/ja304970p | J. Am. Chem. Soc. 2012, 134, 14142−14157

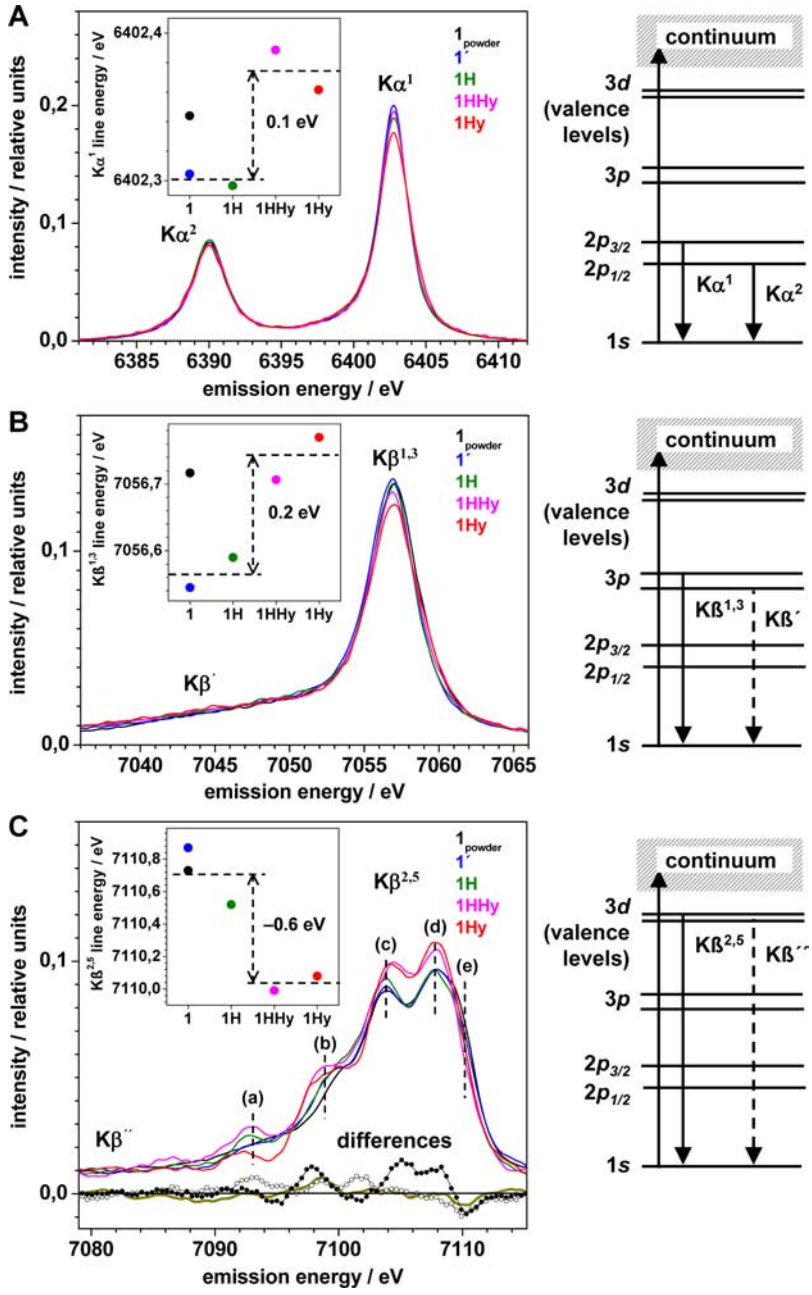


**Figure 5.** X-ray emission line spectra of samples of **1** for nonresonant excitation (left) and underlying electronic transitions (right). All spectra were normalized to unity areas in the shown regions. (A) K$\alpha^{1,2}$ spectra and K$\alpha^{1}$ line energies (from first moment calculations[116] over 6400−6405 eV) in the inset. (B) K$\beta^{1,3}$ and K$\beta'$ emission spectra and K$\beta^{1,3}$ energies (from first moment calculations[116] over 7050−7065 eV) in the inset. (C) K$\beta^{2,5}$ spectra (valence-to-core transitions) and energies of the highest-energy inflection points in the inset (spectra vertically displaced by 0.1 units). The maxima denoted a−e are discussed in the text. The difference spectra were calculated as **1**′−$\mathbf{1}_{\text{powder}}$ (dark yellow line), reflecting dissolution effects; as the average of **1Hy**−**1**′ and **1HHy**−**1H** (●), reflecting hydride binding; and as the average of **1HHy**−**1Hy** and **1H**−**1**′ (○), reflecting adt−N protonation.

by ∼0.2 eV. The K$\alpha^{1}$ and K$\beta^{1,3}$ spectra thus were affected mainly by the hydride binding.

The largest spectral differences were observed in the K$\beta^{2,5}$ emission region (valence-to-core transitions) (Figure 5C). The spectra revealed at least five (a−e) discernible maxima, their relative intensities varying between samples. The spectrum of **1**′ showed only small differences as compared to $\mathbf{1}_{\text{powder}}$, that is, slightly higher intensities around maximum (b) and lower intensities around maximum (d). For protonation at the adt−N, increased maxima (a−c) and a decreased maximum (d) mainly were observed. The binding of a bridging hydride in **1HHy** and **1Hy** resulted in a down-shift by ∼0.6 eV of the emission at the highest energies, as well as pronouncedly increased maxima (b−d) and a decreased maximum (e), in comparison to the hydride-lacking states. These spectral changes became better discernible in the respective difference spectra, reflecting the solvation effects in MeCN, the adt−N protonation, and in particular the bridging hydride binding (Figure 5C, see legend).

**DFT Calculation of Valence-to-Core Transitions (K$\beta^{2,5}$ Emission).** Electronic transitions in the K$\beta^{2,5}$ spectral region were calculated using DFT for the crystal structure and the five


dx.doi.org/10.1021/ja304970p | J. Am. Chem. Soc. 2012, 134, 14142−14157

main solution species of **1** (Figure 6). The calculated stick spectra (Figure 6A, inset; Figure 7) showed about 80

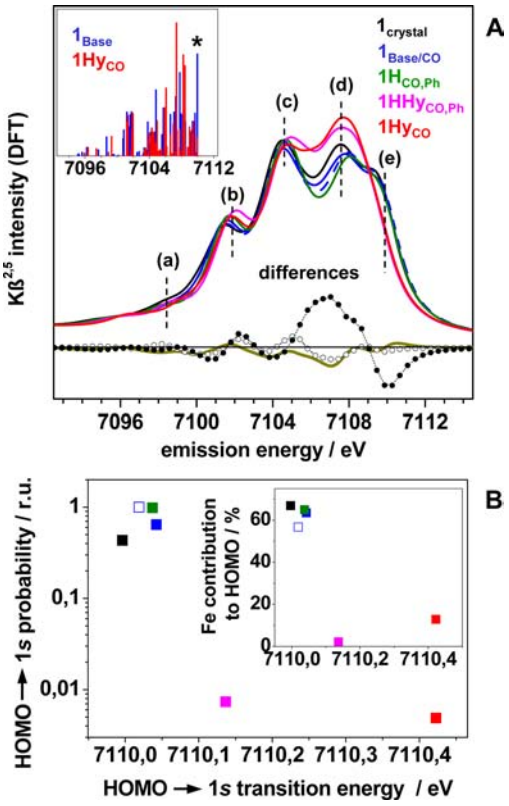


**Figure 6.** K$\beta^{2,5}$ emission spectra calculated by DFT for the structures in Figure 4. Spectra were derived by Gaussian broadening of stick spectra (inset: average of transitions for Fe1 and Fe2; the asterisk marks the HOMO→1s transition); maxima are denoted a–e as for the experimental spectra (Figure 5C); the dashed blue line denotes the $\mathbf{1}_{CO}$ spectrum. The difference spectra were calculated as $\mathbf{1}_{Base}-\mathbf{1}_{crystal}$ (dark yellow line), as the average of $\mathbf{1Hy}_{CO}-\mathbf{1}_{Base}$ and $\mathbf{1HHy}_{CO,Ph}-\mathbf{1H}_{CO,Ph}$ (●), and as the average of $\mathbf{1HHy}_{CO,Ph}-\mathbf{1Hy}_{CO}$ and $\mathbf{1H}_{CO,Ph}-\mathbf{1}_{Base}$ (○). (B) Probabilities (on a logarithmic scale) and energies of HOMO→1s transitions; in the inset, respective contributions of AOs of iron to the HOMO, corresponding to the spectra in (A) (the "□" denote structure $\mathbf{1}_{CO}$; see also Table 2).

transitions from occupied MOs to the 1s level for excitation of each of the two iron atoms, that is, a sum of ~160 transitions in the Kß$^{2,5}$ region. However, about 10 (nonconsecutive) transitions per iron in the region of about 7100–7110 eV contributed more than 50% of the total intensity for all states. The mean transition energies for Fe1 were slightly higher (by 0.01–0.24 eV) as compared to those of Fe2 (Table 2). Comparing transitions at similar energies showed that changes in intensity of decays from only about 10 MOs accounted for most of the calculated spectral differences between Fe1 and Fe2 (Figure 7).

The Kß$^{2,5}$ line shapes that were calculated on the basis of the stick spectra revealed similar apparent maxima (a–e) and reproduced the overall shapes of the experimental spectra well. The energy differences between the electronic transitions, however, apparently were underestimated by ~30% for the used functional/basis-set combination (BP86/TZVP), as judged by comparison between experimental and calculated spectra (compare Figures 5C and 6A). We have previously observed systematic deviations in energy differences of the same size for the use of different functional/basis set combinations in calculations on similar iron compounds.[58] This systematic effect, however, does not influence the conclusions drawn on the electronic structure of **1**.

The DFT-calculated Kß$^{2,5}$ spectra revealed changes similar to those of the experimental spectra, that is, upon dissolution ($\mathbf{1}_{crystal}\rightarrow\mathbf{1}_{Base/CO}$) showing changes of maxima (b,d); upon adt–N protonation ($\mathbf{1}_{Base/CO}/\mathbf{1H}_{CO}\rightarrow\mathbf{1H}_{CO,Ph}/\mathbf{1HHy}_{CO,Ph}$) showing changes of maxima (a–d); and in particular, upon hydride binding ($\mathbf{1}_{Base/CO}/\mathbf{1H}_{CO,Ph}\rightarrow\mathbf{1Hy}_{CO}/\mathbf{1HHy}_{CO,Ph}$) showing changes mainly of maxima (c–e), which is visible in the respective difference spectra (Figure 6A). The good agreement between experimental and calculated Kß$^{2,5}$ lines suggested that the molecular and electronic structure of **1** in all states was reasonably described by the used DFT approach.

A closer inspection of the calculated Kß$^{2,5}$ spectra (sticks) revealed that the observed differences were attributable (i) to shifts in energy of whole emission bands with similar spectral intensities, (ii) to the redistribution of spectral intensity among energy-invariant transitions, and (iii) to the appearance of new transitions. The mean transition energies as compared to $\mathbf{1}_{crystal}$ increased by ~0.5 eV for $\mathbf{1}_{Base/CO}$, increased only by ~0.03 eV for adt–N protonation in $\mathbf{1H}_{CO,Ph}$ and $\mathbf{1HHy}_{CO,Ph}$, but increased by ~0.7 eV for hydride binding ($\mathbf{1Hy}_{CO}$, $\mathbf{1HHy}_{CO,Ph}$) (Table 2). This was accompanied by considerable oscillator strength (probability) changes for transitions at similar energies (Figure 6A, inset; Figure 7), most obvious for the HOMO→1s decay (Figures 6B, 7). Its intensity for the hydride-containing states was less than 1% of the one for the hydride-lacking, unprotonated, or adt–N protonated states. This was unrelated to the transition energies, which were by only 0.1–0.4 eV higher for the hydride states (Figure 6B). The diminished emission at the highest energies in the experimental Kß$^{2,5}$ spectra for the hydride states thus does not reflect a lower HOMO→1s energy, but a strongly decreased transition probability. The HOMO shows contributions from AOs of Fe of up to ~65% for the nonhydride states, but only up to ~15% for the hydride-containing states, for which the ligand-s,p contributions thus were largely increased (Table 2; Figure 6B, inset).

Dissection of the calculated Kß$^{2,5}$ spectra into contributions (i) from the two iron atoms and (ii) from the metal and its ligand species related the emission maxima to the molecular structures (Figure 7). Maximum (e) was dominated by decay from MOs with mostly Fe-d character. Maximum (b) mainly showed CO-s,p contributions of the respective excited Fe1 or Fe2 ions. CO/$PMe_3$-s,p contributions mainly accounted for maximum (c) with relative intensities depending on the protonation state. Maximum (d) showed prominent s,p contributions from the bridging sulfurs; larger $PMe_3$ contributions caused increased intensity for adt–N protonation, which also raised the contributions from the $NCH_2Ph$ moiety around maximum (a). Significant contributions from MOs with prominent hydride character mainly accounted for the large increase of maximum (d) in both **1HHy** and **1Hy** (Figures 6B, 7).

These attributions revealed relations between the molecular and electronic structures. Solvation of **1** in MeCN leads to a redistribution of contributions from $PMe_3$ AOs to MOs at lower energies, to enhanced delocalization of MOs with CO contributions over ligands at both Fe ions, and to a diminished extension of MOs onto the phenyl ring of the dithiolate ligand. CO rotation results in a more similar MO structure for Fe1 and


dx.doi.org/10.1021/ja304970p | J. Am. Chem. Soc. 2012, 134, 14142–14157

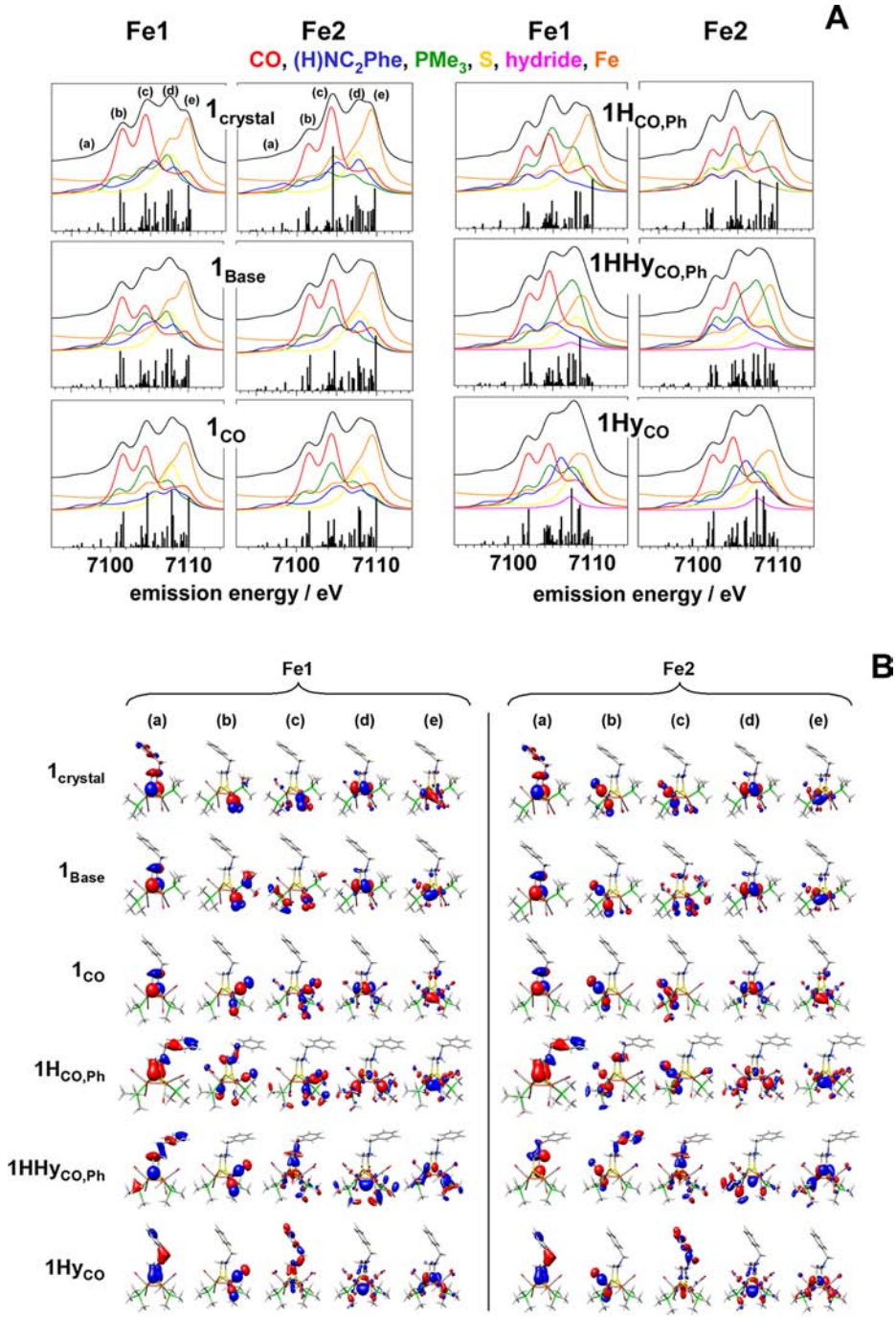


**Figure 7.** (A) K$\beta^{2,5}$ spectra from DFT for the structures of complex **1** in Figure 4 for excitation of Fe1 or Fe2 and (B) corresponding molecular orbitals. In (A), the black lines show K$\beta^{2,5}$ spectra (vertically displaced and scaled for comparison), which represent the sum of the individual contributions from the indicated atoms or groups (colored lines). Respective stick spectra are shown as black bars. The charts in (B) show MOs corresponding to the most intense transitions (largest respective stick) in the spectral regions denoted a–e (as shown for $\mathbf{1}_{crystal}$) in (A).

Fe2, in an increased localization of CO dominated MOs on the ligands of each Fe ion, and in the concentration of emission intensity in fewer transitions. Protonation at the adt–N results in a shift of $PMe_3$ contributions mainly from Fe1 and of $\mu$S contributions to fewer MOs at lower energies, in enhanced contributions of the $NCH_2Ph$ moiety to MOs at low energies, and in enhanced delocalization of CO-dominated MOs.

For bridging hydride binding, the HOMO was less dominated by Fe contributions, and MOs with Fe contributions were more delocalized in $\mathbf{1HHy}_{CO,Ph}$ and $\mathbf{1Hy}_{CO}$. For $\mathbf{1HHy}_{CO,Ph}$, a pronounced shift to higher energies and larger intensities of contributions from the $PMe_3$ groups, as well as significant contributions from AOs of the hydride itself, were observed in addition. $\mathbf{1Hy}_{CO}$ revealed increased contributions from the $NCH_2Ph$ moiety, an even larger new contribution from the hydride to MOs at center energies, and an overall more similar MO structure of Fe1 and Fe2 (Figure 7).

**Pre-edge Absorption in the XANES and DFT on Core-to-Valence Transitions.** Fe K-edge absorption spectra reflect excitations into bound unoccupied electronic levels of, for example, metal-d character. XANES spectra, which were measured using narrow-band K$\alpha$-fluorescence detection, are


dx.doi.org/10.1021/ja304970p | J. Am. Chem. Soc. 2012, 134, 14142–14157

Table 2. Energy Differences of Kß$^{2,5}$ Transitions and Fe-Contributions to the HOMO→1s Decay and to the HOMO from DFT Calculations on Complex 1[a]

| | $\mathbf{1}_{crystal}$ | $\mathbf{1}_{Base}$ | $\mathbf{1}_{CO}$ | $\mathbf{1H}_{CO,Ph}$ | $\mathbf{1HHy}_{CO,Ph}$ | $\mathbf{1Hy}_{CO}$ |
|---|---|---|---|---|---|---|
| $\Delta E$(Kß$^{2,5}$), Fe1−Fe2 [eV] | 0.23 ± 0.01 | 0.16 ± 0.01 | 0.01 ± 0.01 | 0.05 ± 0.02 | 0.20 ± 0.06 | 0.04 ± 0.02 |
| $\Delta E$(Kß$^{2,5}$) between states [eV] | 0 | 0.47 ± 0.05 | 0.52 ± 0.16 | 0.51 ± 0.14 | 1.17 ± 0.02 | 1.21 ± 0.14 |
| Fe-contribution to HOMO→1s [%] | 39.2 | 38.1 | 35.4 | 38.1 | 2.6 | 10.8 |
| Fe1,Fe2-contribution to HOMO [%] | 15.4,51.5 | 21.8,42.6 | 28.9,27.8 | 34.0,30.8 | 0.6,1.6 | 3.1,9.8 |
| Mulliken charge of Fe1,Fe2 | 0.16,0.13 | 0.18,0.13 | 0.15,0.16 | 0.07,0.13 | 0.00,0.01 | 0.03,0.03 |

[a]Mean energy differences ($\Delta E$) of valence-to-core transitions (Kß$^{2,5}$ spectra) between Fe1 and Fe2 and between the crystal structure and the structures for the four solution states were calculated as the average of 80 transitions at the highest energies; the error represents the standard deviation. Contributions from AOs of iron to the HOMO→1s decay were derived from stick spectra (Figure 7). The total Fe character of the HOMO was by ≤10% larger than the Fe-d character. Charges of the iron atoms were derived from Mulliken analysis.

shown in Figure 8. In principle, they correspond to a diagonal transect through the RIXS plane with a spectral width of ∼1 eV (compare to Figure 10). However, the XANES measurements were performed independently to optimize the spectral quality. Because of the higher monochromator resolution and narrow-band Kα detection in the present study, in particular the pre-edge features were considerably better resolved than previously.[49] The overall spectral features of the pre-edge area and main edge rise, however, are similar to the XANES spectra, which were measured using detection of the total X-ray fluorescence (see Figure S5). Notably, the XANES spectra derived from summation over all emission energies in the RIXS plane within noise limits are identical to the total fluorescence spectra (Figure S5).

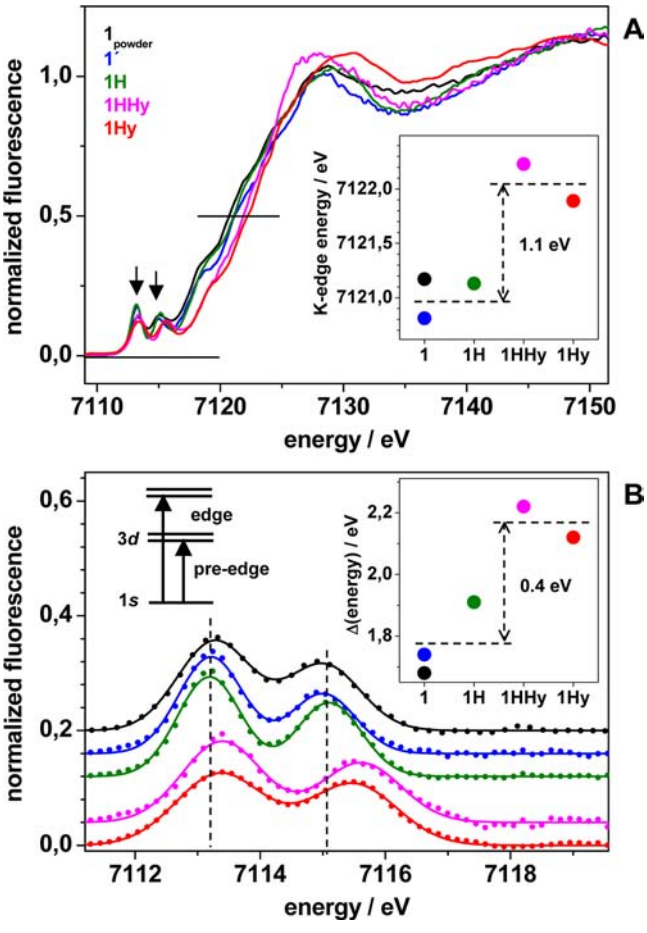


Figure 8. High-resolution XANES spectra measured for a detection energy of 6403 ± 0.5 eV at the Kα$^1$ maximum. (A) Fe K-edge spectra and edge energies, at 50% level of the edge rise, in the inset. The arrows mark the pre-edge peak features. (B) Isolated pre-edge features (dots) from spectra in (A) and energy difference between the two peaks, derived from simulations with the sum of two Gaussians (lines), in the right inset. Spectra were vertically shifted for comparison; vertical dashes emphasize shifts of the peak energies. The left inset sketches the electronic transitions of the excitation process in an atomic level picture.

The K-edge differences between $\mathbf{1}_{powder}$ and $\mathbf{1}'$ presumably reflected solvation effects and CO rotation in a fraction of the $\mathbf{1}'$ sample. Protonation at the adt−N affected the XANES only slightly. A pronounced shift by ∼1.1 eV to higher energies of the K-edge was found for the hydride-containing states (Figure 8A). For all states, two absorption peaks in the pre-edge region were observed (Figure 8B). Their energy difference was slightly larger for $\mathbf{1}'$ as compared to $\mathbf{1}_{powder}$. Protonation at the adt−N resulted in a larger energy difference between the two peaks. Hydride binding caused a shift of both peaks to higher energies, but this shift was much larger, about 0.5 eV, for the second peak (Figure 8B).

The pre-edge region of XANES spectra is attributed to 1s→3d electronic transitions of the metal in an atomic level picture.[92] DFT revealed that this picture only partially explains the pre-edge transitions of **1**. A closer look on the contributing transitions (stick spectra) showed that only the first peak may be considered as a true pre-edge feature (Figure 9A, inset), because it reflects transitions into MOs with up to ∼50% Fe-d character (see the next section), whereas the second peak rather is due to low-lying edge transitions into MOs with mainly CO-s,p character (Figure S3). The calculated pre-edge spectra reproduced the shapes of the experimental spectra and even subtle spectral differences remarkably well (Figures 8B, 9A), that is, an increased energy difference between the two pre-edge peaks in $\mathbf{1}_{Base}$ as compared to $\mathbf{1}_{crystal}$, small changes for adt−N protonation, and considerable shifts to higher energies in the hydride states (Figure 9B). The pre-edge spectra that were calculated for excitation of Fe1 or Fe2 revealed discernible differences in particular for $\mathbf{1}_{crystal}$, $\mathbf{1}_{Base}$, and $\mathbf{1HHy}_{CO,Ph}$ (Figure 9A). CO rotation in $\mathbf{1}_{CO}$ and $\mathbf{1Hy}_{CO}$ resulted in a higher similarity of the spectra for Fe1 and Fe2.

**Kα RIXS Data and Determination of Fe-d Level Energy Splittings.** Improved resolution of transitions into MOs with mostly Fe-d character is expected in resonant inelastic X-ray scattering (RIXS) experiments, that is, for Kα emission recording using resonant excitation of pre-edge transitions, due to diminished lifetime broadening effects.[77,93] Kα RIXS data of complex **1** in its unprotonated state and its three protonation states in MeCN are shown in Figure 10. Transects through the RIXS plane for constant incident energy (CIE)


dx.doi.org/10.1021/ja304970p | J. Am. Chem. Soc. 2012, 134, 14142−14157

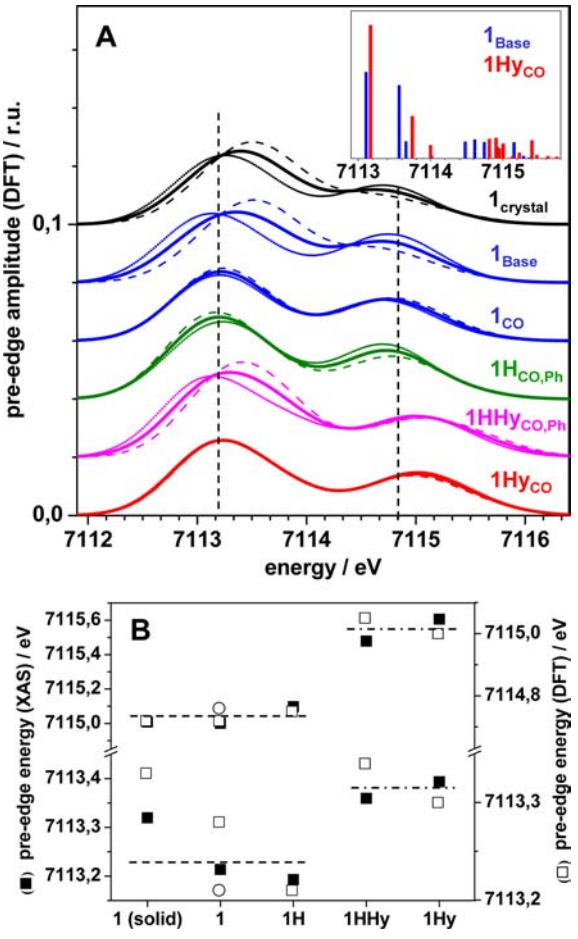


**Figure 9.** Pre-edge transitions of complex **1** calculated by DFT. (A) Calculated spectra (solid lines) for the indicated structures (vertically shifted for comparison) represent the average of spectra for excitation of Fe1 (dashed lines) and Fe2 (dotted lines). Spectra were derived by Gaussian broadening of stick spectra as shown in the inset for $\mathbf{1}_{Base}$ and $\mathbf{1Hy}_{CO}$ (averages of spectra for Fe1 and Fe2). Vertical dashes emphasize peak energy shifts. (B) Comparison of the energies of the two pre-edge peaks from DFT (□, the "○" denotes $\mathbf{1}_{CO}$; right *y*-axis) and experimental spectra (■, left *y*-axis), derived from simulations with two Gaussians of sum spectra in (A) and spectra in Figure 8B. Horizontal dashed and dash-dotted lines mark approximate mean energy levels for the hydride and nonhydride states.

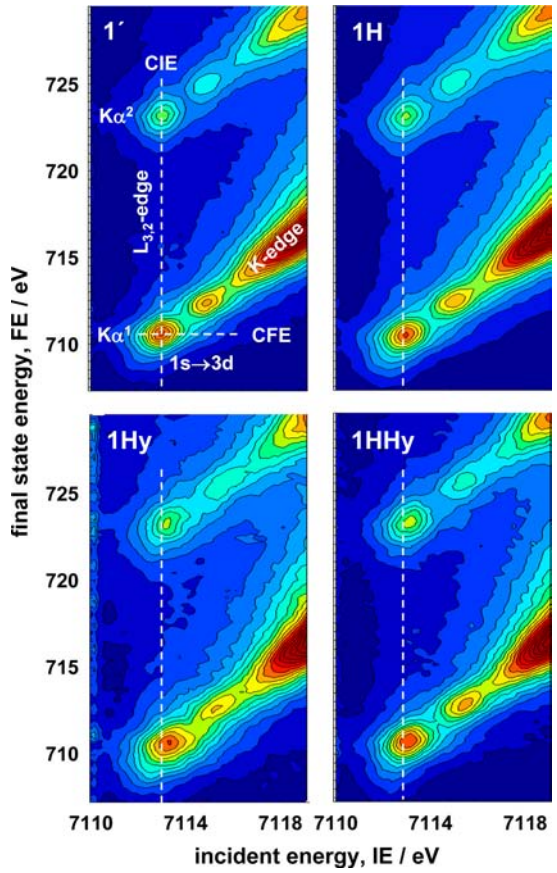


**Figure 10.** Contour plots of $K\alpha^{1,2}$ RIXS data for the four solution states of complex **1**. Dark-blue, lowest values; dark red, highest values of X-ray fluorescence counts. The incident energy (IE, set by the monochromator) is the excitation energy; the final state energy (FE) was calculated as the difference IE minus EE (emission energy, set by the Rowland spectrometer). Dashed lines denote the directions of transects through the RIXS plane corresponding to $L_{3,2}$-edge type spectra (constant incident energy, CIE) or 1s→3d pre-edge spectra (constant final state energy, CFE). Note the energy shifts of the first pre-edge peak in the hydride states.

probe final state configurations ($1s^2 2p^5 3d^{n+1}$), which are similar to those in low-energy L-edge spectroscopy; the resulting spectra thus resemble $L_{3,2}$-edge spectra.[53] For constant final state energies (CFE = incident minus emission energy), the transitions from 1s levels to MOs with Fe-d character become well separated from low-lying edge transitions and the main edge rise. The CIE and CFS spectra of **1** indeed showed narrowing toward Lorentzian line shapes due to the increased spectral resolution (Figure 11A,B).

The CIE spectra of **1** bear resemblance to $L_{3,2}$-edge spectra of low-spin iron species[94,95] (Figure 11A). In particular for the apparent $L_3$-edge absorption (2p→3d transitions) a splitting of the main peak by about 1 eV was observed for the hydride states (**1HHy**, **1Hy**), whereas **1**′ and **1H** rather showed a broader single main peak. A similar peak splitting by ∼1 eV for the hydride states and an upshift by ∼0.2 eV were found in the CFE spectra (Figure 11B), which reflect apparent 1s→3d transitions and correspond to the first pre-edge peak in the XANES (Figure 8). Only small spectral changes were observed for the states protonated at the adt−N.

The underlying structure of MOs with Fe-d contributions was revealed by the DFT calculations of the XAS pre-edge spectra (see the previous section and Figure 11C). The calculated 1s→3d spectra, after the application of Lorentzian broadening of stick spectra, were similar to the experimental CFE spectra for the unprotonated state and all protonation states. The transitions at lowest energies into MOs with mainly Fe-d character on average were by ∼25% more intense in the hydride states, which corresponded to a slight decrease by ∼5% of the Fe-d character of the respective MOs. CO rotation in $\mathbf{1}_{CO}$ and $\mathbf{1Hy}_{CO}$ again caused the transition energies of Fe1 and Fe2 to become more similar as compared to the other states. For all states, transitions into MOs with mainly Fe-d($z^2$) character were at lower energies than transitions into MOs with Fe-d($x^2-y^2$) character (Figure 11C, inset). Accordingly, in an atomic level picture, for the hydride states the peak splitting can be attributed to an increased energy gap between the d($z^2$) and d($x^2-y^2$) levels, mainly due to an increase in the 1s→3d($x^2-y^2$) energy difference. Fitting the experimental spectra by the sum of two Lorentzian functions (Figure 11B) revealed mean


dx.doi.org/10.1021/ja304970p | J. Am. Chem. Soc. 2012, 134, 14142−14157

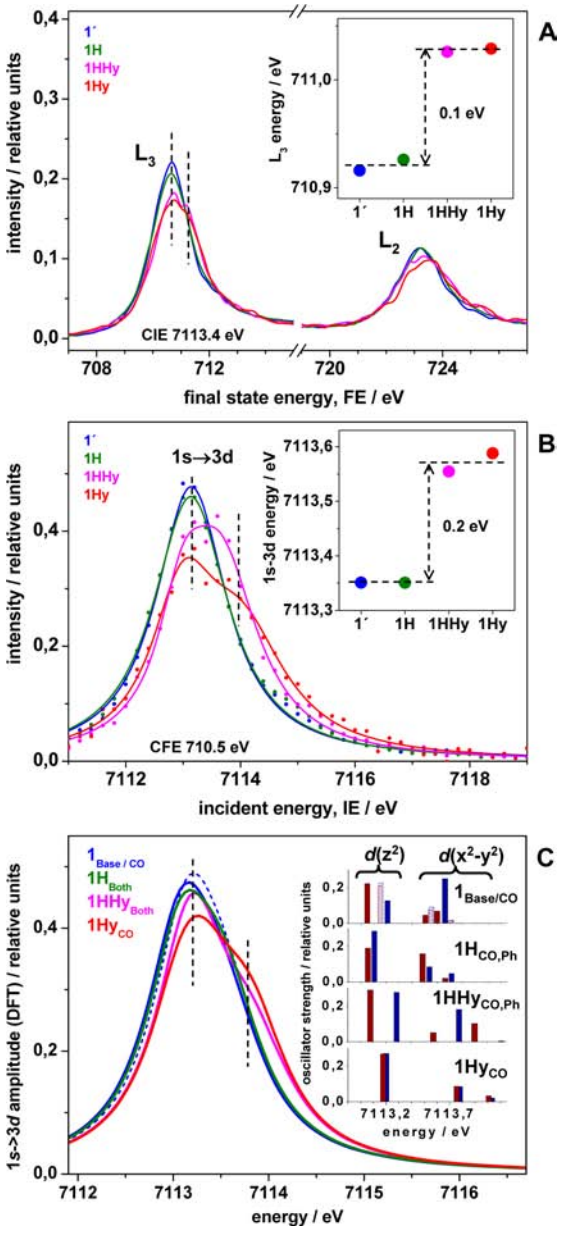


**Figure 11.** Resolution of Fe-d level energy splittings in RIXS data of complex **1**. (A) CIE spectra (IE = 7113.4 ± 0.2 eV) and (B) CFE spectra (FE = 710.5 ± 0.2 eV) for the four indicated samples from data in Figure 10. The insets show mean $L_3$-edge energies (A, derived from first moment calculations[116] in the range of 708−714 eV) and 1s→3d transition energies (B, derived from first moment calculations in the range of 7111.5−7116.0 eV). Lines in (B) show simulations of the experimental data (dots) with sums of two Lorentzians. (C) DFT-calculated pre-edge spectra for the indicated structures (Figure 4, the dashed blue line denotes $\mathbf{1}_{CO}$) derived from Lorentzian broadening of the transitions (stick spectra) shown in the inset (dark blue, Fe1; dark red, Fe2; hatched bars denote $\mathbf{1}_{CO}$; main Fe-d characters of the transitions are indicated). Vertical dashes mark the energy splitting of the main peak in the hydride states best visible for **1Hy**.

energy differences between the apparent Fe-d($z^2$) and Fe-d($x^2-y^2$) levels in reasonable agreement with the values calculated by DFT (Figure 11C, Table 3). For the nonhydride states, the energy difference was about 0.5 eV, whereas for the hydride states the difference was increased to about 0.9 eV on average (Table 3).

**Configuration of Fe-d Orbitals, HOMO/LUMO Energy Gap, and Redox Potentials.** The DFT-calculated energies were plotted versus the Fe-d contents of the MOs with the highest contributions of the five d-orbitals for Fe1 and Fe2 (Figure S4). Protonation of the adt−N or Fe−Fe bond lowered the MO energies by about 1 eV on average; both protonations (in $\mathbf{1HHy}_{CO,Ph}$) lowered the energies by a sum of about 2 eV. The MO energy differences and occupancies tentatively may be translated into apparent, simplified atomic level pictures of the respective Fe-d level degeneracies (Figure S4, insets). For $\mathbf{1}_{crystal}$ and $\mathbf{1}_{Base}$, the d-level configurations resembled an octahedral ($O_h$) Fe(II) for Fe1 and a square-pyramidal ($C_{4v}$) Fe(0) for Fe2 with a lowered d($z^2$) energy as compared to d($x^2-y^2$); CO rotation in $\mathbf{1}_{CO}$ and $\mathbf{1Hy}_{CO}$ caused an inversion of this configuration to yield apparent $C_{4v}$ Fe1(0) and $O_h$ Fe2(II) species; and protonation at the adt−N produced states of both Fe1 and Fe2, which more closely resembled (more oxidized) $O_h$ ions, irrespective of the presence or absence of the hydride in $\mathbf{1H}_{CO,Ph}$ and $\mathbf{1HHy}_{CO,Ph}$.

In principle, the energy difference between the pre-edge absorption at the lowest energy and the Kß$^{2,5}$ emission at the highest energy may allow one to derive an estimate of the energy difference between the LUMO and HOMO levels ($\Delta E_{LH}$).[58] The LUMO and HOMO shapes from DFT are shown in Figure 12A. The LUMO in all cases was mostly located at the Fe ions, showing up to about 55% Fe-d contributions. Fe-d($z^2$) contributions amounted for up to ∼28% and corresponded mainly to Fe1 for all states, except for the ones protonated at the adt−N ($\mathbf{1H}_{CO,Ph}$, $\mathbf{1HHy}_{CO,Ph}$), for which Fe2 contributions prevailed (Table 4). The HOMO was mostly located at iron (≤59%) and dominated by up to ∼20% Fe1- or Fe2-d($z^2$) for the nonhydride states, but located mostly on the phenyl ring ($\mathbf{1HHy}_{CO,Ph}$) or on the adt−NH moiety ($\mathbf{1Hy}_{CO}$) and showing only minor Fe2-d($xy$) contributions for the hydride states (Table 4).

The energy differences of the lowest- and highest-energy inflection points of the pre-edge and Kß$^{2,5}$ spectra (as determined from the first derivative spectra, not shown) were calculated and considered as an approximate measure of the $\Delta E_{LH}$ values. They are compared to the $\Delta E_{LH}$ values calculated by DFT in Figure 12B. For the nonhydride states ($\mathbf{1}_{powder}$, **1′**, **1H**), the experimental and calculated values are rather similar. The mean experimental $\Delta E_{LH}$ for **1′** and **1H** is about 2.0 ± 0.1 eV, and for $\mathbf{1}_{powder}$ it is 2.3 eV. By less than 0.1 eV, larger values were determined from DFT for $\mathbf{1}_{Base/CO}$, $\mathbf{1H}_{CO,Ph}$, and $\mathbf{1}_{crystal}$. For the hydride states, a slightly larger (by ∼0.2 eV for $\mathbf{1HHy}_{CO,Ph}$) or similar (for $\mathbf{1Hy}_{CO}$) $\Delta E_{LH}$ was predicted by DFT. The experimental data suggested a by ∼0.6 eV larger $\Delta E_{LH}$ for the hydride states, which is an overestimation due to

**Table 3. Mean Fe-d Orbital Energy Differences from RIXS and DFT[a]**

| | **1′** ($\mathbf{1}_{Base/CO}$) | **1H** ($\mathbf{1H}_{CO,Ph}$) | **1HHy** ($\mathbf{1HHy}_{CO,Ph}$) | **1Hy** ($\mathbf{1Hy}_{CO}$) |
|---|---|---|---|---|
| $\Delta E$\{d($x^2-y^2$)−d($z^2$)\} [eV] | 0.42 (0.50/0.48) | 0.53 (0.52) | 0.84 (0.66) | 1.03 (0.71) |

[a]Experimental values represent the differences of the peak positions of two Lorentzian curves fitted to the CFE spectra in Figure 11B. Values from DFT (in parentheses) represent the mean differences of energies of the transitions for Fe1 and Fe2 shown in Figure 11C.


dx.doi.org/10.1021/ja304970p | J. Am. Chem. Soc. 2012, 134, 14142−14157

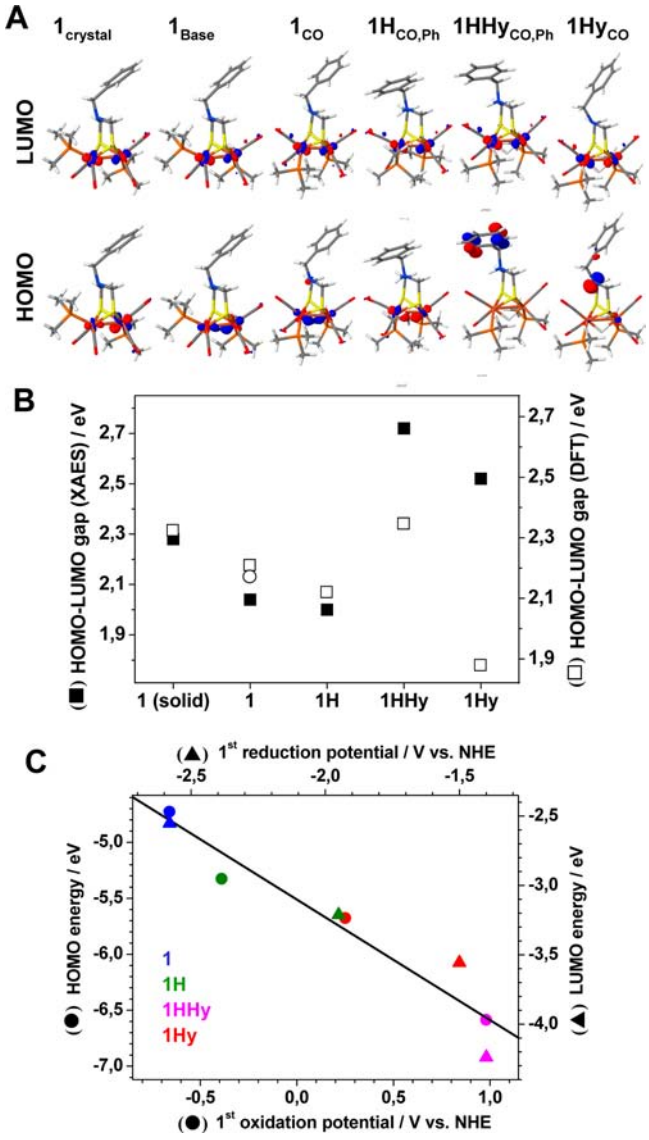


**Figure 12.** HOMO−LUMO energies and redox potentials. (A) Visualization of HOMO and LUMO configurations for the indicated DFT structures. (B) Comparison of LUMO minus HOMO energy differences derived from experimental $K\beta^{2,5}$ emission and pre-edge absorption spectra (left *y*-axis, ■) and from DFT calculations (right *y*-axis, □); the "○" denotes $\mathbf{1}_{CO}$. (C) Plots of the HOMO energy versus the first oxidation potential (circles) and of the LUMO energy versus the first reduction potential (triangles) for the unprotonated states and the three protonated states. Energies were derived from DFT for structures in Figure 4 ($\mathbf{1H}_{CO,Ph}$, $\mathbf{1HHy}_{CO,Ph}$, $\mathbf{1Hy}_{CO}$; blue symbols denote the average over $\mathbf{1}_{Base}$ and $\mathbf{1}_{Co}$), and redox potentials for **1′**, **1H**, **1HHy**, and **1Hy** were taken from ref 52 (NHE, normal hydrogen electrode). The regression line accounts for both data sets (respective axes were scaled accordingly).

the diminished contribution of the HOMO→1s transition to the $K\beta^{2,5}$ spectra (Figure 6B). However, an increased value of $\Delta E_{LH}$ for **1HHy** was found both in the calculated and experimental data (Figure 12B).

In Figure 12C, we show plots of the first oxidation potential versus the HOMO energy and of the first reduction potential versus the LUMO energy for the various states of **1**. The redox potentials have been derived previously from electrochemistry experiments;[52] the HOMO and LUMO energies were calculated here by DFT. Both plots were compatible with an approximately linear relation between the redox potentials and the MO energies. A higher HOMO energy, that is, for $\mathbf{1}_{Base/CO}$ and $\mathbf{1H}_{CO,Ph}$, corresponded to a less positive oxidation potential with respect to the hydride states, and a lower LUMO energy, that is, for $\mathbf{1HHy}_{CO,Ph}$ and $\mathbf{1Hy}_{CO}$, corresponded to a less negative reduction potential as compared to the nonhydride states. In other words, it is easier to extract an electron (oxidation) from a higher-energy HOMO and to insert an (Fe-d) electron (reduction) into a lower-energy LUMO. The redox potentials and MO energies apparently were determined mostly by the total charge of the complexes; that is, successive protonations to add one or two positive charges, in $[\mathbf{1H}]^+$ and $[\mathbf{1Hy}]^+$ or $[\mathbf{1HHy}]^{2+}$, each increased the oxidation/reduction potentials by about 0.7 ± 0.1 V and decreased the HOMO/LUMO energies by about 0.9 ± 0.1 eV on average (Figure 12C).

## ■ DISCUSSION

**Characterization of [FeFe] Active Site Model Compounds by XAES-DFT.** This investigation further establishes XAES in concert with DFT calculations[58,72,76,80,96] as a viable tool to study relations between molecular and electronic structures of transition metal complexes. Here, we have determined the electronic properties of a diiron model complex of the [FeFe] hydrogenase active site in solution. In particular, the binding of a metal-bridging hydride specifically alters the XAES spectra, which is quantitatively reproduced by DFT. This offers a novel method for characterization of metal-hydride species, which are important intermediates in many biological and chemical reactions.[6,97−101] For complex **1**, even protonation at the adt ligand is detectable. XAES-DFT thus may help to decide, for example, whether bridging or/and terminal hydride species are involved in $H_2$ formation in [FeFe] hydrogenases.[102−104]

Ligand isomerizations of [FeFe] complexes in solution influence their reactivity. For complex **1**, structural changes, including Fe−Fe/ligand distance changes, metal site symmetry alterations, and stabilization by hydrogen bonding are involved.[49,52,82] These effects impact on the electronic structure and redox potentials. Good agreement between experimental and DFT-calculated XAES spectral changes supports our assignment of major rotational isomers of complex **1** and the attribution of spectral changes to adt−N protonation and/or

**Table 4. Fe-d Contributions to the HOMO and LUMO in DFT Structures of Complex 1**[a]

| | | $\mathbf{1}_{crystal}$ | $\mathbf{1}_{Base}$ | $\mathbf{1}_{CO}$ | $\mathbf{1H}_{CO,Ph}$ | $\mathbf{1HHy}_{CO,Ph}$ | $\mathbf{1Hy}_{CO}$ |
|---|---|---|---|---|---|---|---|
| total Fe-d contribution [%] | HOMO | 59.0 | 52.7 | 43.4 | 51.6 | 2.1 | 12.4 |
| | LUMO | 45.1 | 54.1 | 49.8 | 50.5 | 52.0 | 51.2 |
| dominant Fe-d contribution [%] | HOMO | Fe2-d($z^2$) 18.4 | Fe2-d($z^2$) 20.0 | Fe1-d($z^2$) 18.0 | Fe1-d($z^2$) 19.5 | Fe2-d($xy$) 1.3 | Fe2-d($xy$) 9.1 |
| | LUMO | Fe1d($z^2$) 26.3 | Fe1d($z^2$) 27.7 | Fe1d($z^2$) 22.7 | Fe2d($z^2$) 26.9 | Fe2d($z^2$) 26.4 | Fe1d($z^2$) 23.0 |

[a]For graphic representations of the HOMO and LUMO shapes, see Figure 12A.


dx.doi.org/10.1021/ja304970p | J. Am. Chem. Soc. 2012, 134, 14142−14157

hydride binding. The inexpensive BP86/TZVP level of DFT[58,72] sufficiently describes the electronic structure of the model complex.

The analysis of Kß-emission XES spectra and of resonant-excitation XAS spectra provides a detailed picture of both occupied and unoccupied MOs, allowing, for example, determination of the spin multiplicity ($M = 2S + 1$). The low emission intensity in the Kß′ region indicates the absence of unpaired spins on the formal Fe(I) ($d^7$) ions in **1**.[53,58,68,71,105] This shows that spin pairing occurs to yield a singlet ground state ($M = 1$), in agreement with previous results for diiron compounds.[58] Accordingly, this multiplicity has been employed in the DFT calculations of the XAS/XES spectra. The simple description is that the d($z^2$) electrons pair to form the metal−metal bond, and the unoccupied orbital is the metal−metal antibond. This is where the simple view in terms of localized Fe centers breaks down for the delocalized electronic structure in a cluster complex.

The configurations of Fe-d dominated MOs of complex **1** suggest considerable electronic asymmetry in the complex, even for the similar $(\mu S)_2(PMe_3)(CO)_2$ first-sphere coordination of the iron atoms and both with or without a bridging hydride. In tendency the iron sites may be considered as varying between species, which to some extent resemble $O_h$ Fe(II) and $C_{4v}$ Fe(0) ions, depending on ligand rotation and protonation. Asymmetry also is evident in the Fe−H bond lengths differing by ∼0.03 Å in $\mathbf{1Hy}_{CO}$, as compared to similar bond lengths in $\mathbf{1HHy}_{CO,Ph}$ (Figure 4). Rather subtle geometry changes may alter the electronic structure to bias hydride binding toward one iron, perhaps leading to more reactive terminal species.[42,106,107]

For low-valence low-spin iron−carbonyl compounds such as **1**, the interpretation of some X-ray spectroscopic features in terms of valence levels needs to be qualified. Formally, **1** is in an $Fe(I)_2$ state when unprotonated, and this changes to $Fe(II)_2H^-$ for hydride binding. Transitions in the K-edge shift to higher energies by up to ∼1 eV for the hydride states, which may suggest an increased Fe oxidation state.[22,49] However, transitions into Fe-d dominated MOs (core-to-valence or "1s→3d" transitions) show only slight energy upshifts. The effective iron oxidation state thus remains almost unchanged upon hydride binding, as supported by the Mulliken charges. The increased energies of transitions into ligand (CO) dominated MOs presumably are explained by the longer Fe−ligand bonds in the 6-coordinated hydride states.

For the unprotonated states of complex **1**, an approximate determination of the HOMO−LUMO energy difference ($\Delta E_{LH}$) was achieved on the basis of the Kß$^{2,5}$ emission and pre-edge absorption spectra. The XAES data as well as the DFT calculations suggest a $\Delta E_{LH}$ of ∼2.3 eV for $\mathbf{1}_{powder}$, which is diminished to ∼2.0 eV in MeCN, for unprotonated or protonated adt−N. A $\Delta E_{LH}$ of ∼2.8 eV was obtained for an asymmetric [FeFe] model.[58] The highest energy Kß$^{2,5}$ feature corresponds to a $1s^2 3d^{n-1}$ final state, while the pre-edge XAS corresponds to a $1s^1 3d^{n+1}$ final state. The later state may have significant contributions from the core hole, whereas the former will not. Multiplet splittings of 1s→3d transitions may thus affect the determined energy gap.[92,94,95] The influence of the core hole has been studied previously by inclusion of an increased nuclear charge in the DFT calculations,[72] and this approximate treatment of electronic relaxation did not improve the agreement between the spectral shapes of theoretical and experimental Kß$^{2,5}$ spectra, but the calculated energies were somewhat altered. That the XAS does have a core hole in the final state represents a fundamental problem for a rigorous comparison of the calculated HOMO−LUMO energies. How the inclusion of core hole effects in evaluations of the XAS spectra affects the energy differences remains to be shown. In any event, in the present study, reasonable agreement between calculated and experimental energy gaps was obtained for the simplest approach, in which the electronic relaxation in the intermediate state is neglected. We have shown previously that multiplet contributions even for Kß$^{1,3}$ detection of XANES spectra may not significantly obscure the determined HOMO−LUMO gap in this class of compounds.[58]

For the hydride states, $\Delta E_{LH}$ estimation is complicated by the diminished contribution of the HOMO→1s transition to the Kß$^{2,5}$ emission. Increased Fe-d character of the HOMO, that is, due to enhanced centro-symmetry of the Fe sites, increasing the dipole-forbidden character of the HOMO→1s transition, did not account for this effect. Presumably, the low metal character of the HOMO in the hydride states reduces the overlap of the vibronic wave functions of the initial ($1s^1HOMO^2$) and final ($1s^2HOMO^1$) states in the radiative decay process. $\Delta E_{LH}$ thus may be overestimated experimentally, yielding an increase in both hydride states. However, DFT reveals an increase to ∼2.3 eV only for **1HHy**, but rather a further slight decrease to ∼1.9 eV for **1Hy**.

The configuration of the metal valence levels (d-orbitals) is intimately related to hydride binding, that is, in hydrogenases.[50,108,109] L-edge spectroscopy in principle can measure d-level splittings, but uses low-energy X-rays and thus is only surface-sensitive.[110] We show that bulk-sensitive Fe K$\alpha$ RIXS allows for the determination of the energy difference between MOs with mainly Fe-d($z^2$) and Fe-d($x^2-y^2$) characters. Apparent mean d−d splittings for the two iron atoms of close to 0.5 eV for the nonhydride states and about 2 times higher values for the hydride states were found and confirmed by DFT. In addition, DFT reveals that the respective MO energies drop by about 1 eV each upon adt−N and Fe−Fe bond protonation, which should be related to the redox potentials of the compound.[111]

Indeed, for **1** we observe correlations between the first oxidation potential and the HOMO energy, as well as between the first reduction potential and the LUMO energy. Presumably, apparent deviations from linearity are attributable to the specific molecular structure of each rotational isomer and protonation species, which influences the MO energies, and to the location, in particular for the HOMO, mostly on the iron atoms or on the bridging dithiolate ligand in the hydride states. The experimental and theoretical determination of the HOMO/LUMO and Fe-d level energies hence may allow one to probe the effects of ligand sphere tuning for minimization of the overpotential in the $H_2$ reactions.[112]

**Relations between the Molecular and Electronic Structures of Complex 1.** Our main findings on the molecular and electronic structures in the various states of complex **1** are summarized as follows.

*Dissolution of Complex 1 in MeCN.* Good agreement between the structural parameters from EXAFS, crystallography, and DFT allows assignment of prevailing rotational isomers of complex **1**. Minor structural changes in **1′** occur, that is, slightly increased Fe−ligand/Fe distances, when the Base rotational configuration as in the crystal is retained in MeCN. However, even these subtle changes cause alterations of the electronic structure. While the HOMO/LUMO shapes and locations mainly on the Fe ions remain about unchanged, a

slight decrease in the HOMO−LUMO gap, increased delocalization of occupied MOs (valence levels) in particular onto the CO ligands, and increased differences between occupied MOs with major Fe1 or Fe2 contributions are observed. As a result, the intrinsic asymmetry of the two iron atoms due to a different geometry of their $(CO)_2(PMe_3)$ ligands is even enhanced in solution.

The other main isomer ($\mathbf{1}_{CO}$) is energetically disfavored. The CO rotation causes a significant elongation of the Fe−Fe distance, similar to **1H**. However, the HOMO/LUMO gap and the redox potentials as compared to $\mathbf{1}_{Base}$ are about unchanged, although the HOMO now is dominated by Fe1. The electronic structure becomes more symmetric in that the occupied MOs are more localized on the respective CO ligands of either Fe1 or Fe2 and the unoccupied MOs (Fe-d levels) exhibit similar energies for both irons. Interestingly, in $\mathbf{1}_{CO}$ an inversion of the apparent symmetry occurs, so that Fe2 is the more symmetric ion with a higher Mulliken charge, whereas in $\mathbf{1}_{Base}$ it is Fe1 (Figure S4). The MO symmetry and d-level configuration of $\mathbf{1}_{CO}$ therefore overall are more similar to $\mathbf{1Hy}_{CO}$ than to $\mathbf{1H}_{CO,Ph}$ or $\mathbf{1HHy}_{CO,Ph}$.

*Protonation at the adt−N Group.* The adt-protonation favors structures showing CO (and Ph) rotation, that is, $\mathbf{1H}_{CO,Ph}$, due to energetic stabilization by hydrogen bonding of the apical CO at Fe1,[49,82] causing significant elongation of the Fe−Fe distance, as in the hydride states. The HOMO/LUMO gap remains about unchanged as compared to **1′**, but the LUMO now is dominated by Fe2, similar to $\mathbf{1HHy}_{CO,Ph}$. However, an energy drop in the valence levels by about 1 eV is calculated, which nicely manifests in more positive reduction/oxidation potentials. The adt−N protonation causes a considerable delocalization of occupied MOs onto the dithiolate bridge, detectable in the Kß$^{2,5}$ spectra. Unoccupied MOs (Fe-d levels) rather are more delocalized onto both Fe ions, resulting in an apparent Fe(II) character and a more symmetric electronic configuration for both Fe1 and Fe2, similar to the hydride states.

*Bridging Hydride Binding.* Protonation of the Fe−Fe bond is well discernible by XAES. In both **1Hy** and **1HHy**, CO rotation is preferred, but Ph rotation also is likely in **1HHy**. This leads to elongated Fe−Fe/ligand distances, reflecting the 6-coordinated iron sites. For both species, the LUMO is similar to the unprotonated states and located on Fe1. The HOMO, however, now is located mostly on the dithiolate bridge. The energy differences between Fe-d($z^2$) and Fe-d($x^2-y^2$) levels are increased, and the hydride causes a ∼1 eV energy drop of the Fe-d orbitals as for adt−N protonation, corresponding to increased redox potentials.

Particularly interesting are occupied MOs with large hydride contributions, which are similar in both species, well visible in the Kß$^{2,5}$ spectra, and reproduced by DFT. The occupied MOs in **1HHy** are more delocalized as compared to **1H** and show rather different shapes for Fe1 and Fe2, whereas they are more localized and more similar for Fe1 and Fe2 in **1Hy** as compared to **1′**. However, the Fe-d dominated MOs of $\mathbf{1HHy}_{CO,Ph}$ suggest an Fe(II) character for both irons as in $\mathbf{1H}_{CO,Ph}$, but a more asymmetric Fe1 as in $\mathbf{1'}_{CO}$ for $\mathbf{1Hy}_{CO}$. The HOMO/LUMO gap thus was increased for **1HHy**, but decreased for **1Hy**, with respect to the hydride-lacking species.

**Mechanistic Considerations.** In [FeFe] hydrogenases, the adt−N group possibly functions as a proton transfer relay to the active site prior to $H_2$ formation.[12,16,19,113] Previous investigations on **1** have suggested that adt−N protonation facilitates bridging hydride binding in this case.[49] By CO rotation and hydrogen bonding, a structure of **1H** is preformed, which supports hydride binding without further energy-costly structural changes.[49,82] In the [FeFe] hydrogenase, however, $H_2$ formation may not involve a bridging but a terminal hydride.[12,16,19,113] On the other hand, in the [FeFe] model complexes, bridging hydride species often represent low-energy states, leading to low turnover rates.[35,42,106] Our present results further qualify the mechanistic concept of facilitated hydride binding in **1**.

Apparently, two routes to bridging hydride species exist in principle (Scheme 1). (1) The adt−N protonation in the $\mathbf{1}_{Base}\rightarrow\mathbf{1H}_{CO,Ph}$ transition induces a structure similar to $\mathbf{1HHy}_{CO,Ph}$, showing an elongated, solvent-exposed Fe−Fe bond and a H-bond between the adt−N and apical CO at Fe1. Also, the electronic structure, featuring a rather symmetric MO configuration for both iron ions, partly is preformed to adopt the hydride, and this leads to similar Fe−H bond lengths for Fe1 and Fe2 in $\mathbf{1HHy}_{CO,Ph}$. (2) A second pathway may be opened by the $\mathbf{1}_{Base}\rightarrow\mathbf{1}_{CO}$ rotation without adt−N protonation. The structure of $\mathbf{1'}_{CO}$ also features an exposed Fe−Fe bond, but a more asymmetric electronic structure of the Fe ions, similar to $\mathbf{1Hy}_{CO}$, which leads to different Fe−H bond lengths. Experimentally, both hydride states have been found to be formed via initial adt−N protonation, and no direct formation has been observed thus far.[52] However, in a more general sense, ligand rotation rather than hydride binding may limit product formation in [FeFe] compounds in certain situations. In the case of complex **1**, both hydride states are energetically highly stabilized, explaining the low rate of $H_2$ formation in this system.[82]

**Scheme 1. Two Pathways for Facilitated Bridging Hydride Binding in Compound 1**[a]

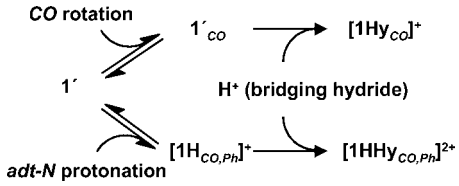


[a]Protonation at the adt−N group or CO-rotation (of the $(PMe_3)(CO)_2$ ligands at Fe1) leads to species showing molecular and electronic properties, which are preformed to be similar to the respective hydride states, thereby facilitating subsequent protonation of the Fe−Fe bond.

## CONCLUSIONS

We have shown that XAES-DFT analysis facilitates characterization of rotational isomers, ligand protonation, and hydride binding in solution and qualitative and quantitative interpretation of the resulting molecular and electronic changes for the [FeFe] hydrogenase model complex **1**. This characterization approach may open new routes to the verification of the effects of built-in modifications to overcome mechanistic bottlenecks under reaction conditions, thus to the determination of direct relations between the molecular and electronic structures and the reactivity and reaction paths, and ultimately to the iterative improvement of [FeFe] catalysts by guided synthesis approaches for hydrogen cleavage and proton reduction to produce $H_2$.

## ■ ASSOCIATED CONTENT

### Supporting Information

(1) EXAFS analysis of **1** (Figure S1, Table S1), (2) rotational isomers in MeCN (Figure S2), (3) MOs for the second pre-edge peak (Figure S3), (4) apparent Fe-d orbital configurations (Figure S4), and (5) comparison of narrow-band and total-fluorescence detected XANES (Figure S5). This material is available free of charge via the Internet at http://pubs.acs.org.

## ■ AUTHOR INFORMATION


### Corresponding Author

michael.haumann@fu-berlin.de


### Notes

The authors declare no competing financial interest.

## ■ ACKNOWLEDGMENTS

Financial support from the Deutsche Forschungsgemeinschaft (DFG; grant Ha3265/3-1 and funding within the Unicat Cluster of Excellence Berlin to M.H.), the Swedish Research Council, the Knut and Alice Wallenberg Foundation, the Swedish Energy Agency (to S.O.), and the European Union (FP7, Energy 212508, SOLAR-H2 consortium) is gratefully acknowledged. K.G.V.H. thanks "Stiftelsen Bengt Lundqvist minne" and the Wenner-Gren Foundation for fellowships. M.H. thanks the DFG for a Heisenberg fellowship. We thank Drs. T.-C. Weng, K. Kvashnina, and P. Glatzel at beamline ID26 for excellent support and the ESRF for granting of a Long Term Project (to M.H.).

## ■ REFERENCES


(1) Nocera, D. G. *Inorg. Chem.* **2009**, *48*, 10001−10017.
(2) Hammarström, L.; Winkler, J. R.; Gray, H. B.; Styring, S. *Science* **2011**, *333*, 288.
(3) Gust, D.; Moore, T. A.; Moore, A. L. *Acc. Chem. Res.* **2009**, *42*, 1890−1898.
(4) Lubitz, W.; Reijerse, E. J.; Messinger, J. *Energy Environ. Sci.* **2008**, *1*, 15−31.
(5) Bensaid, S.; Centi, G.; Garrone, E.; Perathoner, S.; Saracco, G. *ChemSusChem* **2012**, *5*, 500−521.
(6) Rakowski DuBois, M.; DuBois, D. L. *Chem. Soc. Rev.* **2009**, *38*, 62−72.
(7) Le Goff, A.; Artero, V.; Jousselme, B.; Tran, P. D.; Guillet, N.; Metaye, R.; Fihri, A.; Palacin, S.; Fontecave, M. *Science* **2009**, *326*, 1384−1387.
(8) Schlögl, R. *ChemSusChem* **2010**, *3*, 209−222.
(9) Corr, M. J.; Murphy, J. A. *Chem. Soc. Rev.* **2011**, *40*, 2279−2292.
(10) Fontecilla-Camps, J. C.; Volbeda, A.; Cavazza, C.; Nicolet, Y. *Chem. Rev.* **2007**, *107*, 4273−4303.
(11) Mulder, D. W.; Shepard, E. M.; Meuser, J. E.; Joshi, N.; King, P. W.; Posewitz, M. C.; Broderick, J. B.; Peters, J. W. *Structure* **2011**, *19*, 1038−1052.
(12) Stripp, S. T.; Happe, T. *Dalton Trans.* **2009**, 9960−9969.
(13) Ghirardi, M. L.; Posewitz, M. C.; Maness, P. C.; Dubini, A.; Yu, J.; Seibert, M. *Annu. Rev. Plant Biol.* **2007**, *58*, 71−91.
(14) Vignais, P. M.; Colbeau, A. *Curr. Issues Mol. Biol.* **2004**, *6*, 159−188.
(15) Peters, J. W.; Lanzilotta, W. N.; Lemon, B. J.; Seefeldt, L. C. *Science* **1998**, *282*, 1853−1858.
(16) Nicolet, Y.; Lemon, B. J.; Fontecilla-Camps, J. C.; Peters, J. W. *Trends Biochem. Sci.* **2000**, *25*, 138−143.
(17) Roseboom, W.; De Lacey, A. L.; Fernandez, V. M.; Hatchikian, E. C.; Albracht, S. P. *J. Biol. Inorg. Chem.* **2006**, *11*, 102−118.
(18) Silakov, A.; Kamp, C.; Reijerse, E.; Happe, T.; Lubitz, W. *Biochemistry* **2009**, *48*, 7780−7786.
(19) Silakov, A.; Wenk, B.; Reijerse, E.; Lubitz, W. *Phys. Chem. Chem. Phys.* **2009**, *11*, 6592−6599.
(20) Erdem, O. F.; Schwartz, L.; Stein, M.; Silakov, A.; Kaur-Ghumaan, S.; Huang, P.; Ott, S.; Reijerse, E. J.; Lubitz, W. *Angew. Chem., Int. Ed.* **2011**, *50*, 1439−1443.
(21) Stripp, S. T.; Goldet, G.; Brandmayr, C.; Sanganas, O.; Vincent, K. A.; Haumann, M.; Armstrong, F. A.; Happe, T. *Proc. Natl. Acad. Sci. U.S.A.* **2009**, *106*, 17331−17336.
(22) Lambertz, C.; Leidel, N.; Havelius, K. G.; Noth, J.; Chernev, P.; Winkler, M.; Happe, T.; Haumann, M. *J. Biol. Chem.* **2011**, *286*, 40614−40623.
(23) (a) Bruska, M. K.; Stiebritz, M. T.; Reiher, M. *J. Am. Chem. Soc.* **2011**, *133*, 20588−20603. (b) Stiebritz, M. T.; Reiher, M. *Chem. Sci.* **2012**, *3*, 1739−1751.
(24) Knörzer, P.; Silakov, A.; Foster, C. E.; Armstrong, F. A.; Lubitz, W.; Happe, T. *J. Biol. Chem.* **2012**, *287*, 1489−1499.
(25) Kuchenreuther, J. M.; Grady-Smith, C. S.; Bingham, A. S.; George, S. J.; Cramer, S. P.; Swartz, J. R. *PLoS One* **2010**, *5*, e15491.
(26) Darensbourg, M. Y.; Lyon, E. J.; Smee, J. J. *Coord. Chem. Rev.* **2000**, *206*, 533−561.
(27) Rauchfuss, T. B. *Science* **2007**, *316*, 553−554.
(28) Darensbourg, M. Y. *Comments Inorg. Chem.* **2010**, *31*, 144−152.
(29) Tard, C.; Pickett, C. J. *Chem. Rev.* **2009**, *109*, 2245−2274.
(30) Darensbourg, M. Y. *Nature* **2005**, *433*, 589−591.
(31) Lomoth, R.; Kaur-Ghumaan, S.; Schwartz, L.; Stein, M.; Ott, S. *Angew. Chem., Int. Ed.* **2010**, *49*, 8033−8036.
(32) Tard, C.; Liu, X.; Ibrahim, S. K.; Bruschi, M.; De Gioia, L.; Davies, S. C.; Yang, X.; Wang, L. S.; Sawers, G.; Pickett, C. J. *Nature* **2005**, *433*, 610−613.
(33) Gloaguen, F.; Lawrence, J. D.; Rauchfuss, T. B.; Benard, M.; Rohmer, M. M. *Inorg. Chem.* **2002**, *41*, 6573−6582.
(34) Rauchfuss, T. B. *Inorg. Chem.* **2004**, *43*, 14−26.
(35) Gloaguen, F.; Rauchfuss, T. B. *Chem. Soc. Rev.* **2009**, *38*, 100−108.
(36) Lomoth, R.; Ott, S. *Dalton Trans.* **2009**, 9952−9959.
(37) Felton, G. A. N.; Mebi, C. A.; Petro, B. J.; Vannucci, A. K.; Evans, D. H.; Glass, R. S.; Lichtenberger, D. L. *J. Organomet. Chem.* **2009**, *694*, 2681−2699.
(38) Camara, J. M.; Rauchfuss, T. B. *Nat. Chem.* **2012**, *4*, 26−30.
(39) Jablonskyte, A.; Wright, J. A.; Pickett, C. J. *Dalton Trans.* **2010**, *39*, 3026−3034.
(40) Wright, J. A.; Webster, L.; Jablonskyte, A.; Woi, P. M.; Ibrahim, S. K.; Pickett, C. J. *Faraday Discuss.* **2011**, *148*, 359−371.
(41) Wang, N.; Wang, M.; Liu, J.; Jin, K.; Chen, L.; Sun, L. *Inorg. Chem.* **2009**, *48*, 11551−11558.
(42) Barton, B. E.; Rauchfuss, T. B. *Inorg. Chem.* **2008**, *47*, 2261−2263.
(43) Cheah, M. H.; Borg, S. J.; Best, S. P. *Inorg. Chem.* **2007**, *46*, 1741−1750.
(44) Surawatanawong, P.; Tye, J. W.; Darensbourg, M. Y.; Hall, M. B. *Dalton Trans.* **2010**, *39*, 3093−3104.
(45) Ezzaher, S.; Gogoll, A.; Bruhn, C.; Ott, S. *Chem. Commun.* **2010**, *46*, 5775−5777.
(46) Zampella, G.; Fantucci, P.; De Gioia, L. *J. Am. Chem. Soc.* **2009**, *131*, 10909−10917.
(47) Felton, G. A. N.; Mebi, C. A.; Petro, B. J.; Vannucci, A. K.; Evans, D. H.; Glass, R. S.; Lichtenberger, D. L. *J. Organomet. Chem.* **2009**, *694*, 2681−2699.
(48) Yu, L.; Greco, C.; Bruschi, M.; Ryde, U.; De Gioia, L.; Reiher, M. *Inorg. Chem.* **2011**, *50*, 3888−3900.
(49) Löscher, S.; Schwartz, L.; Stein, M.; Ott, S.; Haumann, M. *Inorg. Chem.* **2007**, *46*, 11094−11105.
(50) Foerster, S.; van Gastel, M.; Brecht, M.; Lubitz, W. *J. Biol. Inorg. Chem.* **2005**, *10*, 51−62.
(51) Brecht, M.; Gastel, M. v.; Buhrke, T.; Friedrich, B.; Lubitz, W. *J. Am. Chem. Soc.* **2003**, *125*, 13075−13083.
(52) Eilers, G.; Schwartz, L.; Stein, M.; Zampella, G.; de Gioia, L.; Ott, S.; Lomoth, R. *Chemistry* **2007**, *13*, 7075−7084.
(53) Glatzel, P.; Bergmann, U. *Coord. Chem. Rev.* **2005**, *249*, 65−95.

(54) De Groot, F.; Kotani, A. *Core Level Spectroscopy of Solids*; Taylor & Francis CRC Press: Boca Raton, FL, 2008.
(55) de Groot, F. *Chem. Rev.* **2001**, *101*, 1779−1808.
(56) Dau, H.; Haumann, M. *Coord. Chem. Rev.* **2008**, *252*, 273−295.
(57) Strange, R. W.; Feiters, M. C. *Curr. Opin. Struct. Biol.* **2008**, *18*, 609−616.
(58) Leidel, N.; Chernev, P.; Havelius, K. G.; Ezzaher, S.; Ott, S.; Haumann, M. *Inorg. Chem.* **2012**, *51*, 4546−4559.
(59) Bergmann, U.; Glatzel, P.; Robblee, J. H.; Messinger, J.; Fernandez, C.; Cinco, R.; Visser, H.; McFarlane, K.; Bellacchio, E.; Pizarro, S.; Sauer, K.; Yachandra, V. K.; Klein, M. P.; Cox, B. L.; Nealson, K. H.; Cramer, S. P. *J. Synchrotron Radiat.* **2001**, *8*, 199−203.
(60) Namatame, H.; Fujimori, A.; Takagi, H.; Uchida, S.; de Groot, F. M.; Fuggle, J. C. *Phys. Rev. B: Condens. Matter* **1993**, *48*, 16917−16925.
(61) Abbate, M.; Fuggle, J. C.; Fujimori, A.; Tjeng, L. H.; Chen, C. T.; Potze, R.; Sawatzky, G. A.; Eisaki, H.; Uchida, S. *Phys. Rev. B: Condens. Matter* **1993**, *47*, 16124−16130.
(62) Grioni, M.; van Acker, J. F.; Czyzyk, M. T.; Fuggle, J. C. *Phys. Rev. B: Condens. Matter* **1992**, *45*, 3309−3318.
(63) Weijs, P. J.; van Leuken, H.; de Groot, R. A.; Fuggle, J. C.; Reiter, S.; Wiech, G.; Buschow, K. H. *Phys. Rev. B: Condens. Matter* **1991**, *44*, 8195−8203.
(64) de Groot, F. M.; Fuggle, J. C.; Thole, B. T.; Sawatzky, G. A. *Phys. Rev. B: Condens. Matter* **1990**, *42*, 5459−5468.
(65) Glatzel, P.; Jacquamet, L.; Bergmann, U.; de Groot, F. M. F.; Cramer, S. P. *Inorg. Chem.* **2002**, *41*, 3121−3127.
(66) Yamaoka, H.; Oura, M.; Taguchi, M.; Morikawa, T.; Takahiro, K.; Terai, A.; Kawatsura, K.; Vlaicu, A. M.; Ito, Y.; Mukoyama, T. *J. Phys. Soc. Jpn.* **2004**, *73*, 3182−3191.
(67) Badro, J.; Struzhkin, V. V.; Shu, J. F.; Hemley, R. J.; Mao, H. K.; Kao, C. C.; Rueff, J. P.; Shen, G. Y. *Phys. Rev. Lett.* **1999**, *83*, 4101−4104.
(68) Degroot, F. M. F.; Fontaine, A.; Kao, C. C.; Krisch, M. *J. Phys.: Condens. Matter* **1994**, *6*, 6875−6884.
(69) Peng, G.; Wang, X.; Randall, C. R.; Moore, J. A.; Cramer, S. P. *Appl. Phys. Lett.* **1994**, *65*, 2527−2529.
(70) Peng, G.; Degroot, F. M. F.; Hamalainen, K.; Moore, J. A.; Wang, X.; Grush, M. M.; Hastings, J. B.; Siddons, D. P.; Armstrong, W. H.; Mullins, O. C.; Cramer, S. P. *J. Am. Chem. Soc.* **1994**, *116*, 2914−2920.
(71) Zaharieva, I.; Chernev, P.; Risch, M.; Gerencser, L.; Berggren, G.; Shevchenko, G.; Anderlund, M.; Weng, T.-C.; Haumann, M.; Dau, H. *J. Phys. Conf. Ser.* **2009**, *190*, 012141−012146.
(72) Lee, N.; Petrenko, T.; Bergmann, U.; Neese, F.; DeBeer, S. *J. Am. Chem. Soc.* **2010**, *132*, 9715−9727. Smolentsev, G.; Soldatov, A. V.; Messinger, J.; Merz, K.; Weyhermüller, T.; Bergmann, U.; Pushkar, Y.; Yano, J.; Yachandra, V. K.; Glatzel, P. *J. Am. Chem. Soc.* **2009**, *131*, 13161−13167.
(73) Chandrasekaran, P.; Stieber, S. C. E.; Collins, T. J.; Que, L.; Neese, F.; DeBeer, S. *Dalton Trans.* **2011**, *40*, 11070−11079.
(74) George, S. D.; Petrenko, T.; Neese, F. *J. Phys. Chem. A* **2008**, *112*, 12936−12943.
(75) George, S. D.; Berry, J. F.; Aliaga-Alcalde, N.; Petrenko, T.; Bill, E.; Mienert, B.; Sturhahn, W.; Wieghardt, K.; Neese, F. *J. Am. Chem. Soc.* **2007**, *233*, 455−455.
(76) Leidel, N.; Popovic-Bijelic, A.; Havelius, K. G.; Chernev, P.; Voevodskaya, N.; Gräslund, A.; Haumann, M. *Biochim. Biophys. Acta* **2012**, *1817*, 430−444.
(77) de Groot, F. M.; Glatzel, P.; Bergmann, U.; van Aken, P. A.; Barrea, R. A.; Klemme, S.; Havecker, M.; Knop-Gericke, A.; Heijboer, W. M.; Weckhuysen, B. M. *J. Phys. Chem. B* **2005**, *109*, 20751−20762.
(78) Pollock, C. J.; DeBeer, S. *J. Am. Chem. Soc.* **2011**, *133*, 5594−5601.
(79) Lancaster, K. M.; Finkelstein, K. D.; DeBeer, S. *Inorg. Chem.* **2011**, *50*, 6767−6774.
(80) Lancaster, K. M.; Roemelt, M.; Ettenhuber, P.; Hu, Y.; Ribbe, M. W.; Neese, F.; Bergmann, U.; DeBeer, S. *Science* **2011**, *334*, 974−977.
(81) Delgado-Jaime, M. U.; Dible, B. R.; Chiang, K. P.; Brennessel, W. W.; Bergmann, U.; Holland, P. L.; DeBeer, S. *Inorg. Chem.* **2011**, *50*, 10709−10717.
(82) Schwartz, L.; Eilers, G.; Eriksson, L.; Gogoll, A.; Lomoth, R.; Ott, S. *Chem. Commun.* **2006**, 520−522.
(83) Dau, H.; Liebisch, P.; Haumann, M. *Anal. Bioanal. Chem.* **2003**, *376*, 562−583 ; http://leonardo.phys.washington.edu/feff/.
(84) Neese, F. *Orca: An ab-initio, DFT, and semiempirical electronic structure package. V.2.7.0*; Max-Planck Institute for Chemical Energy Conversion: Mülheim, Germany, available at: http://www.thch.uni-bonn.de/tc/orca/.
(85) Becke, A. D. *Phys. Rev. A* **1988**, *38*, 3098.
(86) Perdew, J. P. *Phys. Rev. B* **1986**, *33*, 8822.
(87) Kim, K.; Jordan, K. D. *J. Phys. Chem.* **1994**, *98*, 10089−10094.
(88) Schäfer, A.; Huber, C.; Ahlrichs, R. *J. Chem. Phys.* **1994**, *100*, 5829−5835.
(89) Sinnecker, S.; Rajendran, A.; Klamt, A.; Diedenhofen, M.; Neese, F. *J. Phys. Chem. A* **2006**, *110*, 2235−2245 ; http://www.asiinstr.com/technical/Dielectric%20Constants.htm.
(90) Mulliken, R. S. *J. Chem. Phys.* **1955**, *23*, 1833−1840.
(91) DeBeer George, S.; Petrenko, T.; Neese, F. *J. Phys. Chem. A* **2008**, *112*, 12936−12943.
(92) Westre, T. E.; Kennepohl, P.; DeWitt, J. G.; Hedman, B.; Hodgson, K. O.; Solomon, E. I. *J. Am. Chem. Soc.* **1997**, *119*, 6297−6314. Hocking, R. K.; DeBeer George, S.; Gross, Z.; Walker, F. A.; Hodgson, K. O.; Hedman, B.; Solomon, E. I. *Inorg. Chem.* **2009**, *48*, 1678−1688.
(93) Hayashi, H. *Anal. Sci.* **2008**, *24*, 15−23.
(94) Wasinger, E. C.; Groot, F. M. F. d.; Hedman, B.; Hodgson, K. O.; Solomon, E. I. *J. Am. Chem. Soc.* **2003**, *125*, 12894−12906.
(95) Hocking, R. K.; Wasinger, E. C.; de Groot, F. M.; Hodgson, K. O.; Hedman, B.; Solomon, E. I. *J. Am. Chem. Soc.* **2006**, *128*, 10442−10451.
(96) DeBeer, S.; Beckwith, M. A.; Roemelt, M.; Collomb, M. N.; DuBoc, C.; Weng, T. C.; Bergmann, U.; Glatzel, P.; Neese, F. *Inorg. Chem.* **2011**, *50*, 8397−8409.
(97) Lubitz, W.; Tumas, W. *Chem. Rev.* **2007**, *107*, 3900−3903.
(98) Nagel, Z. D.; Klinman, J. P. *Chem. Rev.* **2006**, *106*, 3095−3118.
(99) de Jongh, P. E.; Adelhelm, P. *ChemSusChem* **2010**, *3*, 1332−1348.
(100) Besora, M.; Lledos, A.; Maseras, F. *Chem. Soc. Rev.* **2009**, *38*, 957−966.
(101) McGrady, G. S.; Guilera, G. *Chem. Soc. Rev.* **2003**, *32*, 383−392.
(102) Nicolet, Y.; de Lacey, A. L.; Vernede, X.; Fernandez, V. M.; Hatchikian, E. C.; Fontecilla-Camps, J. C. *J. Am. Chem. Soc.* **2001**, *123*, 1596−1601.
(103) Liu, Z. P.; Hu, P. *J. Am. Chem. Soc.* **2002**, *124*, 5175−5182.
(104) Bruschi, M.; Fantucci, P.; De Gioia, L. *Inorg. Chem.* **2003**, *42*, 4773−4781.
(105) Sakurai, K.; Eba, H.; Numako, C.; Iihara, J. *Anal. Chem.* **2000**, *72*, 2613−2617.
(106) De Gioia, L.; Zampella, G.; Fantucci, P. *Chem. Commun.* **2010**, *46*, 8824−8826.
(107) Ezzaher, S.; Capon, J. F.; Gloaguen, F.; Petillon, F. Y.; Schollhammer, P.; Talarmin, J.; Pichon, R.; Kervarec, N. *Inorg. Chem.* **2007**, *46*, 3426−3428.
(108) Stein, M.; Lubitz, W. *Curr. Opin. Chem. Biol.* **2002**, *6*, 243−249.
(109) Bruschi, M.; Greco, C.; Fantucci, P.; De Gioia, L. *Inorg. Chem.* **2008**, *47*, 6056−6071.
(110) Achkar, A. J.; Regier, T. Z.; Monkman, E. J.; Shen, K. M.; Hawthorn, D. G. *Sci. Rep.* **2011**, *1*, 182.
(111) Roy, L. E.; Batista, E. R.; Hay, P. J. *Inorg. Chem.* **2008**, *47*, 9228−9237.
(112) Armstrong, F. A.; Hirst, J. *Proc. Natl. Acad. Sci. U.S.A.* **2011**, *108*, 14049−14054.
(113) Peters, J. W. *Curr. Opin. Struct. Biol.* **1999**, *9*, 670−676.
(114) Stripp, S.; Sanganas, O.; Happe, T.; Haumann, M. *Biochemistry* **2009**, *48*, 5042−5049.

(115) Lubitz, W.; Reijerse, E.; van Gastel, M. *Chem. Rev.* **2007**, *107*, 4331−4365.
(116) Messinger, J.; Robblee, J. H.; Bergmann, U.; Fernandez, C.; Glatzel, P.; Visser, H.; Cinco, R. M.; McFarlane, K. L.; Bellacchio, E.; Pizarro, S. A.; Cramer, S. P.; Sauer, K.; Klein, M. P.; Yachandra, V. K. *J. Am. Chem. Soc.* **2001**, *123*, 7804−7820.